ELSEVIER

Engineering Analysis with Boundary Elements 25 (2001) 535–556

ENGINEERING ANALYSIS *with* BOUNDARY ELEMENTS

www.elsevier.com/locate/enganabound

A new error indicator based on stresses for three-dimensional elasticity

K.H. Muci-Küchler[a,*], J.C. Miranda-Valenzuela[b]

[a]*University of Detroit Mercy, Detroit, MI 48219-0900, USA*
[b]*Wessex Institute of Technology, Ashurst Lodge, Ashurst, Southampton SO40 7AA, UK*

Received 2 June 2000; revised 21 November 2000; accepted 15 January 2001

Abstract

As of now, most of the error indicators available for elastostatic problems are computed in terms of quantities that do not necessarily have the most relevant physical meaning from the point of view of a mechanical engineer. Furthermore, only few of them have been extended to three-dimensional problems where all the advantages of the boundary element method (BEM) over other numerical techniques are more evident. In this work, a new efficient and reliable error indicator for three-dimensional elastostatic problems is presented based on ideas previously developed by the authors for the two-dimensional case. This error indicator directly estimates the error in the numerical solution for the boundary stresses and exploits in its formulation the high accuracy in the nodal values for those quantities provided by Hermite-like higher order boundary elements. The basic idea behind the computation of the new error indicator is to compare, on an element-by-element basis, two different numerical solutions. The first solution is obtained from an analysis using Hermite-like elements. The second one is obtained by using some of the degrees of freedom of the Hermite-like elements to approximate the field variables inside the elements using conventional Lagrangian shape functions. In this sense, it is assumed that the bigger the difference among these two solutions, the bigger the error in the stresses computed with the Hermite-like elements. Since both solutions are obtained from just one analysis, the computational cost of the proposed error indicator is very low. Three numerical examples are presented to show that the results obtained using this new error indicator with an-*h*-adaptive strategy are satisfactory and very promising.

Keywords: Adaptive meshing; Error estimation; Hermite boundary elements; Hypersingular boundary integral equations

1. Introduction

The accuracy of the numerical solutions obtained with the boundary element method (BEM) strongly depends on how the boundary of the domain is discretized. The number, type, and distribution of the elements that constitute the mesh are factors that have an important effect on the quality of the approximate solution provided by the method. In general, all the decisions regarding the construction of the mesh are based solely on the experience and knowledge of the analyst. However, different techniques have been developed to improve the discretization of the boundary selectively in an automatic fashion. These techniques are commonly known as *adaptive meshing techniques*.

In recent years, the number of publications regarding adaptive meshing techniques in the BEM has increased significantly, and most of the research work has been focused on the formulation and implementation of new and more reliable error indicators. In Refs. [1,2], a comprehensive list of contributions up to 1994 is provided. Since then, other alternatives have appeared. In what follows, a brief explanation of some of the most relevant ones is presented.

Charafi et al. [3] used the local reanalysis technique to implement an efficient *h*-hierarchical adaptive meshing technique. They proposed a local enrichment scheme to obtain an improved solution for each element of the mesh. The improved solution was compared with the original one in order to obtain an estimate of the error in the numerical solution inside the element.

Guiggiani [4] used the direct differentiation approach to perform a sensitivity analysis of approximate boundary element solutions with respect to the position of the collocation points. In a similar approach, Paulino et al. [5], used the rate of change of the tractions and generalized displacements with respect to the positions of middle nodes of quadratic boundary elements as error indicators. These rates of change were calculated by direct analytic differentiation of the governing equations for the problem. Gallego, et al. [6] extended the work of Guiggiani [4] presenting sensitivity analysis of the solutions for the hypersingular boundary integral equation (HBIE) in the potential problem. In order to obtain the sensitivity equations, the derivative

* Corresponding author.
E-mail address: mucikh@udmercy.edu (K.H. Muci-Küchler).

0955-7997/01/$ - see front matter
PII: S0955-7997(01)00016-9

with respect to the position of the collocation point of the HBIE was evaluated.

In Ref. [7], Paulino et al. proposed the evaluation of the residual of the HBIEs as an error indicator. This methodology was developed for the approximation of the error on the boundary as well as in the interior of the domain. Liang et al. [8], employed a modified version of the error indicator proposed by Paulino et al. combining the residuals of the Conventional Boundary Integral Equations (CBIEs) and HBIEs for the computation of error indicators. Menon et al. [9] presented a basic iteration scheme that consisted of using the CBIEs for solving the boundary value problem and iterating this solution with the HBIEs. A residual was defined as the difference in the derivative quantities, and this residual was used as a BEM error estimate.

Muci-Küchler et al. [10], Muci-Küchler and Miranda-Valenzuela [11] and Miranda-Valenzuela et al. [12] presented formulations for the computation of error indicators for Hermite elements [13–16] in two-dimensional potential, elastostatic, and thermoelastostatic problems, respectively. These error indicators were based on the possibility of obtaining two different numerical solutions for the tangential derivatives of the field variables from just one analysis with Hermite elements. The comparison of the two solutions inside an element was used as an estimate of the error for that element.

Despite the considerable number of references available regarding adaptive meshing and error estimation in the BEM, only a few have addressed three-dimensional problems. This may come as a direct consequence of the increased complexity encountered in the three-dimensional implementation of the method. Nevertheless, it seems surprising since it is in three-dimensional problems where the advantages of the reduced dimensionality of the BEM are more evident.

In three-dimensional problems, the use of the residual as an error indicator has been widespread. In 1987, Cerrolaza and Alarcon [17] used a residual type error indicator and hierarchical shape functions to implement a *p*-adaptive method for three-dimensional potential problems. This type of problem was also addressed by Liapis [18], who implemented *h*-refinement and *h*-regeneration schemes using the residual as an error indicator. The residual was also used by Crook and Smith [19] to implement an *h*-adaptive BEM using continuous and discontinuous elements in three-dimensional elastostatic problems. Ervin and Stephan [20] used the Galerkin BEM to implement an *h*-adaptive BEM for solving three-dimensional electrostatic plate problems. In their work, the residual was also chosen as the error indicator. Demkowicz et al. [21] used the residual to implement a Galerkin *hp* BEM for the solution of elastic scattering problems in linear acoustics.

In addition to the use of the residual as an error indicator, other approaches were followed by Karafiat [22], Yokoyama and Zhan [23] and Bächtold et al. [25]. Continuing the previous work by Demkowicz et al. [21], Karafiat considered the errors caused by interpolation of functions, geometry and incident wave to formulate an a priori convergence estimate for the three-dimensional Helmholtz exterior problem. Yokoyama and Zhan used the convergence characteristics of the ratio of the integral of the squared error to the integral of the squared exact value to implement a self-adaptive method for the determination of element degree in three-dimensional elastostatic problems. This approach was extended further by Yokoyama and Kanoh [24], who included the zooming method in their formulation. Finally, Bächtold et al. [25] extended the sample error analysis proposed by Kamiya and Kawaguchi [26] to solve three-dimensional electrostatic problems.

In this work, the ideas presented in Ref. [11] are extended to three-dimensional elastostatic problems. The computation of the error indicator proposed here involves the comparison, on an element-by-element basis, of two numerical solutions for the boundary stresses obtained from functional representations with different numbers of degrees of freedom. It is assumed that the larger the difference between these two numerical solutions, the larger the error inside the element. One of the advantages of this approach is the possibility to estimate the error directly in the stresses, which are, in most cases, the quantity of interest for the designers of mechanical components.

In order to keep the computational cost at a minimum, both solutions are obtained from just one analysis with Hermite-like higher order boundary elements, which include the nodal values of the tangential derivatives of the field variables in the functional representation used for those quantities inside the elements. The first solution is obtained using all the degrees of freedom of the element together with the corresponding higher order shape functions. The second, less accurate solution, is obtained by using only the conventional degrees of freedom (the nodal values of the field variables) and Lagrangian shape functions. As will be seen later, the difference between these two solutions can be used to reasonably estimate the error in the original solution with Hermite-like elements.

In three dimensions, Muci-Küchler and Rudolphi [27] presented the implementation of Hermite-like higher order boundary elements in the context of three-dimensional elastostatic problems. In their formulation, second derivatives of the field variables at the functional nodes were not considered as first suggested by Watson [13]. Although this scheme does not guarantee C^1 continuity along the element faces, it does not seem to compromise the stability of the BEM as reported by Tomlinson et al. [28].

Pullan and Bradley [29] presented a different approach. In the case of the potential problem, Pullan and Bradley showed that it is possible to obtain a formulation for Hermite elements that includes the nodal values of the cross-derivatives. However, they point out that apparently it is not always possible to keep a consistent Hermitian representation of the geometry or the field variables and,

under those circumstances, the use of transition elements may be needed.

Without any loss of generality, in this work Hermite-like higher order boundary elements are implemented as suggested by Muci-Küchler and Rudolphi and used to formulate a reliable and efficient error indicator for three-dimensional elastostatic problems.

2. BEM formulation

The formulation of Hermite-like higher order boundary elements for three-dimensional problems requires the coincident collocation of the CBIEs and the Tangent Derivative Boundary Integral Equations (TDBIEs). In what follows, the CBIEs and TDBIEs for three-dimensional elastostatic problems are presented together with brief descriptions of how the Hermite-like elements are formulated and how the boundary stresses can be computed.

2.1. Conventional boundary integral equations

Consider a three-dimensional closed domain V bounded by a surface S. Assuming that there are no body forces acting inside the domain, the displacement representation integral for three-dimensional elastostatic problems can be written as [30]

$$u_i(\vec{\xi}) = \int_S [U_{ij}(\vec{x},\vec{\xi})t_j(\vec{x}) - T_{ij}(\vec{x},\vec{\xi})u_j(\vec{x})]\,\mathrm{d}S(\vec{x}), \tag{1}$$

where $\vec{x} = (x_1, x_2, x_3)$ and $\vec{\xi} = (\xi_1, \xi_2, \xi_3)$ denote the field and source points, u_i and t_i are the displacement and traction components, and the kernels U_{ij} and T_{ij} correspond to the fundamental solution displacement and traction tensors. For the case of a homogeneous and isotropic material, the fundamental tensors are given by

$$U_{ij}(\vec{x},\vec{\xi}) = \frac{1}{16\pi\mu(1-\nu)}\left(\frac{1}{r}\right)[(3-4\nu)\delta_{ij} + r_{,i}r_{,j}], \tag{2}$$

$$T_{ij}(\vec{x},\vec{\xi}) = \frac{-1}{8\pi(1-\nu)}\left(\frac{1}{r^2}\right) \times \left\{\frac{\partial r}{\partial n}[(1-2\nu)\delta_{ij} + 3r_{,i}r_{,j}] + (1-2\nu)(r_{,j}n_i - r_{,i}n_j)\right\}, \tag{3}$$

where $T_{ij} = E_{jklm}n_k(\partial U_{il}/\partial x_m)$, and $E_{ijkl} = \lambda\delta_{ij}\delta_{kl} + \mu(\delta_{ik}\delta_{jl} + \delta_{il}\delta_{jk})$ is the fourth order material property tensor describing the elastic medium. Lame's constants are denoted by λ and μ, ν is Poisson's ratio, n_i are the components of the unit outward normal to the boundary S at the field point $\vec{x}$, $r = |\vec{x} - \vec{\xi}|$ is the distance between the source and the field point, $r_i = x_i - \xi_i$ are the components of the position vector $\vec{r} = \vec{x} - \vec{\xi}$, and $r_{,i} = \partial r/\partial x_i$.

After carrying out a regularization process like the one presented in Ref. [31], Eq. (1) can be written as

$$\int_S T_{ij}(\vec{x},\vec{\xi})[u_j(\vec{x}) - u_j(\vec{\xi})]\,\mathrm{d}S(\vec{x}) = \int_S U_{ij}(\vec{x},\vec{\xi})t_j(\vec{x})\,\mathrm{d}S(\vec{x}). \tag{4}$$

If the displacement components are continuous in the vicinity of the source point $\vec{\xi}$, the difference $u_i(\vec{x}) - u_i(\vec{\xi})$ is $O(r)$ in the limit as $r \to 0$ and, therefore, the integrands in the above expression contain only weak $O(1/r)$ singularities.

2.2. Tangent derivative boundary integral equations

To determine the TDBIEs in three-dimensions, some geometry-related quantities need to be defined. Let $\hat{v}$ denote the unit outward normal to the boundary S at the source point $\vec{\xi}$, and let $(\hat{\zeta}_1, \hat{\zeta}_2, \hat{\zeta}_3 = \hat{v})$ be a proper orthonormal basis as shown in Fig. 1. The two unit tangent vectors $\hat{\zeta}_1$ and $\hat{\zeta}_2$ can be arbitrarily chosen as long as they satisfy the condition $\hat{\zeta}_1 \times \hat{\zeta}_2 = \hat{v}$. The direction cosines of the basis vectors $\hat{\zeta}_1$, $\hat{\zeta}_2$, and $\hat{\zeta}_3$ with respect to the underlying rectangular coordinate system (x_1,x_2,x_3) will be determined and denoted by $l_{ij} = \hat{\zeta}_i \cdot \hat{\imath}$.

Also, in the sequel, ϵ_{ijk} will be the three-dimensional unit pseudotensor (whose only non-zero components are given

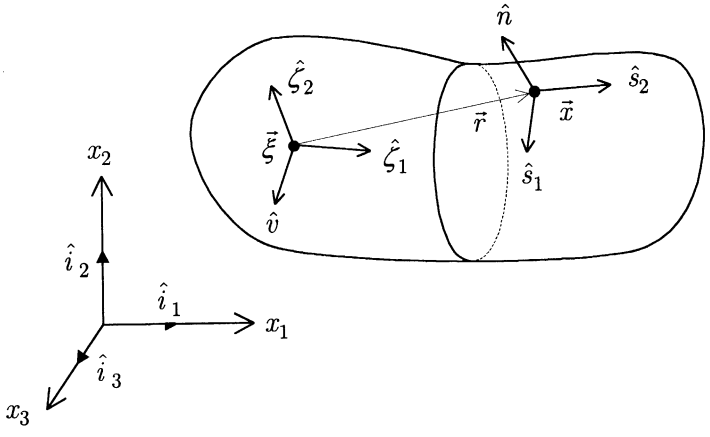

Fig. 1. Three-dimensional domain and coordinate system.

by $\epsilon_{123} = \epsilon_{231} = \epsilon_{312} = 1$ and $\epsilon_{132} = \epsilon_{321} = \epsilon_{213} = -1$), $\epsilon_{\alpha\beta}$ will denote the two-dimensional unit pseudotensor ($\epsilon_{11} = \epsilon_{22} = 0$, $\epsilon_{12} = -\epsilon_{21} = 1$), and it is understood that the range of the Greek indices is only from 1 to 2 and that the summation convention is in force.

To obtain the form of the interior representation of the displacement gradients that leads to the TDBIEs, the operation

$$(\hat{\zeta}_\beta \times \hat{\nu})\cdot\nabla_{\vec{\xi}} = \epsilon_{pqk} v_q l_{\beta p} \frac{\partial}{\partial \xi_k} \tag{5}$$

is applied to Eq. (1) and use is made of certain identities pertaining to the fundamental tensors and their derivatives to regularize the resulting expressions. The final equation can be written as [27]

$$\begin{aligned}
&\int_s V_{\beta ij}(\vec{x},\vec{\xi})\left[u_j(\vec{x}) - u_j(\vec{\xi}) - \frac{\partial u_j}{\partial \zeta_\alpha}(\vec{\xi}) l_{\alpha l} r_l\right] \mathrm{d}S(\vec{x}) \\
&\quad + \int_S Y_{\beta ij\alpha}(\vec{x},\vec{\xi})\, \mathrm{d}S(\vec{x}) \frac{\partial u_j}{\partial \zeta_\alpha}(\vec{\xi}) \\
&\quad = \int_S [W^0_{\beta ij}(\vec{x},\vec{\xi}) t_j(\vec{x}) - W_{\beta ij}(\vec{x},\vec{\xi}) t_j(\vec{\xi})]\, \mathrm{d}S(\vec{x}),
\end{aligned} \tag{6}$$

where the kernels $V_{\beta ij}$, and $Y_{\beta ij\alpha}$, and $W^0_{\beta ij}$ are given by

$$\begin{aligned}
V_{\beta ij}(\vec{x},\vec{\xi}) &= -\epsilon_{\beta\gamma} l_{\gamma k} \frac{\partial T_{ij}}{\partial \xi_k}(\vec{x},\vec{\xi}) \\
&= \begin{cases} -l_{2k} \dfrac{\partial T_{ij}}{\partial \xi_k}(\vec{x},\vec{\xi}) & \text{for } \beta = 1, \\ l_{1k} \dfrac{\partial T_{ij}}{\partial \xi_k}(\vec{x},\vec{\xi}) & \text{for } \beta = 2, \end{cases}
\end{aligned} \tag{7}$$

$$\begin{aligned}
Y_{\beta ij\alpha}(\vec{x},\vec{\xi}) &= l_{\beta p}\epsilon_{pqk} E_{mnjl}[v_q n_n(\vec{x}) - n_q(\vec{x}) v_n] \frac{\partial U_{im}}{\partial \xi_k}(\vec{x},\vec{\xi}) l_{\alpha l} \\
&= \lambda l_{\alpha j}[n_m(\vec{x}) W^0_{\beta im}(\vec{x},\vec{\xi}) - v_m W_{\beta im}(\vec{x},\vec{\xi})] \\
&\quad + \mu l_{\alpha m} n_m(\vec{x}) W^0_{\beta ij}(\vec{x},\vec{\xi}) + \mu l_{\alpha m}[n_j(\vec{x}) W^0_{\beta im}(\vec{x},\vec{\xi}) \\
&\quad - v_j W_{\beta im}(\vec{x},\vec{\xi})],
\end{aligned} \tag{8}$$

$$\begin{aligned}
W_{\beta ij}(\vec{x},\vec{\xi}) &= l_{\beta p}\epsilon_{pqk} n_q(\vec{x}) \frac{\partial U_{ij}}{\partial \xi_k}(\vec{x},\vec{\xi}) \\
&= [\vec{\zeta}_\beta \times \hat{n}(\vec{x})]\cdot \hat{\imath}_k \frac{\partial U_{ij}}{\partial \xi_k}(\vec{x},\vec{\xi}),
\end{aligned} \tag{9}$$

$$\begin{aligned}
W^0_{\beta ij}(\vec{x},\vec{\xi}) &= l_{\beta p}\epsilon_{pqk} v_q(\vec{x}) \frac{\partial U_{ij}}{\partial \xi_k}(\vec{x},\vec{\xi}) \\
&= \begin{cases} -l_{2k} \dfrac{\partial U_{ij}}{\partial \xi_k}(\vec{x},\vec{\xi}) & \text{for } \beta = 1, \\ l_{1k} \dfrac{\partial U_{ij}}{\partial \xi_k}(\vec{x},\vec{\xi}) & \text{for } \beta = 2 \end{cases}.
\end{aligned} \tag{10}$$

From the above expressions it can be seen that the kernel $V_{\beta ij}$ is $O(1/r^3)$ or hypersingular in the limit as $r \to 0$, $W_{\beta ij}$ and $W^0_{\beta ij}$ are both strongly singular or $O(1/r^2)$, and $Y_{\beta ij\alpha}$ is weakly singular or $O(1/r)$ provided that the boundary S has a continuous outward normal at $\vec{\xi}$. However, if at the source point $\vec{\xi}$ the displacements have Hölder continuous first derivatives, if the tractions are continuous, and if the geometry is smooth at the source point $\vec{\xi}$, all the terms in Eq. (6) will contain at most weak $O(1/r)$ singularities.

2.3. Hermite-like boundary elements

Hermite elements were first introduced by Watson in 1986 to solve elastostatic and fracture mechanics problems in two-dimensions [13]. These types of elements have two main characteristics: first, the inclusion of the nodal values of the tangential derivatives of the field variables as degrees of freedom; second, they provide C^1 continuity across element boundaries.

To ensure C^1 continuity across element faces in three-dimensional problems, Hermite boundary elements must include in the functional representation for the displacements more degrees of freedom than the ones corresponding to the nodal values of u_i, $\partial u_i/\partial s_1$, and $\partial u_i/\partial s_2$. Similarly, if the same type of functional representation is used for the tractions, it must include more degrees of freedom than the ones corresponding to the nodal values of t_i, $\partial t_i/\partial s_1$, and $\partial t_i/\partial s_2$. Unfortunately, the inclusion of these additional degrees of freedom is usually difficult to implement. As a reference, the reader can find in Ref. [37] a detailed discussion regarding the shape functions and degrees of freedom that can be used for the functional representation of the field variables for the case of two-dimensional C^1 continuous finite elements.

In this paper, the term *Hermite-like boundary elements* is used to designate all those higher order boundary elements, which only include in their formulation the nodal values of the field variables and their tangential derivatives as the degrees of freedom associated with the element. As mentioned above, these elements cannot guarantee C^1 continuity along element faces and thus, strictly speaking, are not Hermite elements.

Non-isoparametric Hermite-like boundary elements for three-dimensional problems were first implemented by Muci-Küchler and Rudolphi [27]. In their formulation, the nodal values of the field variables and their tangential derivatives were included as degrees of freedom in the functional representation for the displacements and the tractions. Also, the geometry of the elements was represented using the standard shape functions corresponding to Lagrangian elements. Muci-Küchler and Rudolphi reported that, in general, the Hermite-like elements gave better results than Lagrangian elements for the same computational cost.

Following the approach presented in Ref. [27], when Hermite-like boundary elements are used, any field variable

w is approximated inside an element by

$$w(\eta_1,\eta_2)=\sum_{N=1}^{NN}\left\{H_0^{(N)}(\eta_1,\eta_2)w^{(N)}+H_1^{(N)}(\eta_1,\eta_2)\frac{\partial w^{(N)}}{\partial s_1^{(N)}}+H_2^{(N)}(\eta_1,\eta_2)\frac{\partial w^{(N)}}{\partial s_2^{(N)}}\right\}, \tag{11}$$

where η_1 and η_2 are the local or intrinsic coordinates, $H_k^{(N)}$ $(k=0,1,2)$ are the shape functions associated with the Nth functional node, and $s_1^{(N)}$ and $s_2^{(N)}$ correspond to two particular orthogonal tangent directions associated with the Nth functional node that are such that $\hat{s}_1^{(N)}\times\hat{s}_2^{(N)}=\hat{n}^{(N)}$.

It is important to point out that shape functions $H_0^{(N)}$, $H_1^{(N)}$, and $H_2^{(N)}$ in Eq. (11) must satisfy all the following conditions

$$H_0^{(N)}(\eta_1^{(J)},\eta_2^{(J)})=\begin{cases}1 & \text{for } J=N,\\ 0 & \text{for } J\neq N,\end{cases} \tag{12}$$

$$\frac{\partial H_0^{(N)}}{\partial s_1^{(J)}}(\eta_1^{(J)},\eta_2^{(J)})=\frac{\partial H_0^{(N)}}{\partial s_2^{(J)}}(\eta_1^{(J)},\eta_2^{(J)})=0 \qquad \text{for all } J,$$

$$\frac{\partial H_1^{(N)}}{\partial s_1^{(J)}}(\eta_1^{(J)},\eta_2^{(J)})=\begin{cases}1 & \text{for } J=N,\\ 0 & \text{for } J\neq N,\end{cases} \tag{13}$$

$$H_1^{(N)}(\eta_1^{(J)},\eta_2^{(J)})=\frac{\partial H_1^{(N)}}{\partial s_2^{(J)}}(\eta_1^{(J)},\eta_2^{(J)})=0 \qquad \text{for all } J,$$

$$\frac{\partial H_2^{(N)}}{\partial s_2^{(J)}}(\eta_1^{(J)},\eta_2^{(J)})=\begin{cases}1 & \text{for } J=N,\\ 0 & \text{for } J\neq N,\end{cases} \tag{14}$$

$$H_2^{(N)}(\eta_1^{(J)},\eta_2^{(J)})=\frac{\partial H_2^{(N)}}{\partial s_1^{(J)}}(\eta_1^{(J)},\eta_2^{(J)})=0 \qquad \text{for all } J.$$

As will be seen later, the shape functions $H_0^{(N)}$, $H_1^{(N)}$, and $H_2^{(N)}$ for Hermite-like boundary elements can be obtained from the geometry-independent parent shape functions $\hat{H}_0^{(N)}$, $\hat{H}_1^{(N)}$, and $\hat{H}_2^{(N)}$ that satisfy the following conditions

$$\hat{H}_0^{(N)}(\eta_1^{(J)},\eta_2^{(J)})=\begin{cases}1 & \text{for } J=N,\\ 0 & \text{for } J\neq N,\end{cases} \tag{15}$$

$$\frac{\partial \hat{H}_0^{(N)}}{\partial \eta_1}(\eta_1^{(J)},\eta_2^{(J)})=\frac{\partial \hat{H}_0^{(N)}}{\partial \eta_2}(\eta_1^{(J)},\eta_2^{(J)})=0 \qquad \text{for all } J,$$

$$\frac{\partial \hat{H}_1^{(N)}}{\partial \eta_1}(\eta_1^{(J)},\eta_2^{(J)})=\begin{cases}1 & \text{for } J=N,\\ 0 & \text{for } J\neq N,\end{cases} \tag{16}$$

$$\hat{H}_1^{(N)}(\eta_1^{(J)},\eta_2^{(J)})=\frac{\partial \hat{H}_1^{(N)}}{\partial \eta_2}(\eta_1^{(J)},\eta_2^{(J)})=0 \qquad \text{for all } J,$$

$$\frac{\partial \hat{H}_2^{(N)}}{\partial \eta_2}(\eta_1^{(J)},\eta_2^{(J)})=\begin{cases}1 & \text{for } J=N,\\ 0 & \text{for } J\neq N,\end{cases} \tag{17}$$

$$\hat{H}_2^{(N)}(\eta_1^{(J)},\eta_2^{(J)})=\frac{\partial \hat{H}_2^{(N)}}{\partial \eta_1}(\eta_1^{(J)},\eta_2^{(J)})=0 \qquad \text{for all } J.$$

As an example, the geometry-independent shape functions corresponding to the completely discontinuous quadrilateral Hermite-like boundary element are presented in Appendix A.

The shape functions $H_0^{(N)}$, $H_1^{(N)}$ and $H_2^{(N)}$ are obtained from the geometry-independent parent shape functions $\hat{H}_0^{(N)}$, $\hat{H}_1^{(N)}$, and $\hat{H}_2^{(N)}$ through the following relationships [27]:

$$H_0^{(N)}(\eta_1,\eta_2)=\hat{H}_0^{(N)}(\eta_1,\eta_2), \tag{18}$$

$$H_1^{(N)}(\eta_1,\eta_2)=\frac{1}{A^{(N)}}\{A_{22}^{(N)}\hat{H}_1^{(N)}(\eta_1,\eta_2)-A_{21}^{(N)}\hat{H}_2^{(N)}(\eta_1,\eta_2)\},$$

$$H_2^{(N)}(\eta_1,\eta_2)=\frac{1}{A^{(N)}}\{A_{11}^{(N)}\hat{H}_2^{(N)}(\eta_1,\eta_2)-A_{12}^{(N)}\hat{H}_1^{(N)}(\eta_1,\eta_2)\}, \tag{19}$$

where $A=A_{11}A_{22}-A_{12}A_{21}$, the superindex $^{(N)}$ is used to specify quantities evaluated at the Nth functional node, and

$$\begin{bmatrix}A_{11} & A_{12}\\ A_{21} & A_{22}\end{bmatrix}=\frac{1}{G}\begin{bmatrix}(g_{22}\vec{e}_1-g_{12}\vec{e}_2)\cdot\hat{s}_1 & (g_{11}\vec{e}_2-g_{21}\vec{e}_1)\cdot\vec{s}_1\\ (g_{22}\vec{e}_1-g_{12}\vec{e}_2)\cdot\hat{s}_2 & (g_{11}\vec{e}_2-g_{21}\vec{e}_1)\cdot\hat{s}_2\end{bmatrix}. \tag{20}$$

In the above expression, $\vec{e}_\alpha=(\partial x_i/\partial\eta_\alpha)\vec{i}_i$ are the basis vectors related to the local coordinates η_α, $g_{\alpha\beta}=\vec{e}_\alpha\cdot\vec{e}_\beta$ denote 'surface components' of the metric tensor, and $G=\det([g_{\alpha\beta}])$.

2.4. Computation of stresses

Once the boundary element solution for the problem under consideration has been obtained, the displacement components u_i, the tractions components t_i, and the stresses at any point on the boundary S can be determined through the use of the functional representation for the displacements and the tractions employed inside the elements.

To use the standard tensor notation, a local system of rectangular Cartesian coordinates (x_1',x_2',x_3') is introduced at the particular point under consideration, and the orthonormal basis $(\hat{s}_1,\hat{s}_2,\hat{n})$ is identified with the basis $(\hat{\imath}_1',\hat{\imath}_2',\hat{\imath}_3')$ of the primed system as shown in Fig. 2.

Denoting the displacements components in terms of the local coordinate system as u_i', the ϵ_{11}', $\epsilon_{12}'=\epsilon_{21}'$, and ϵ_{22}' components of the strain tensor at the point under

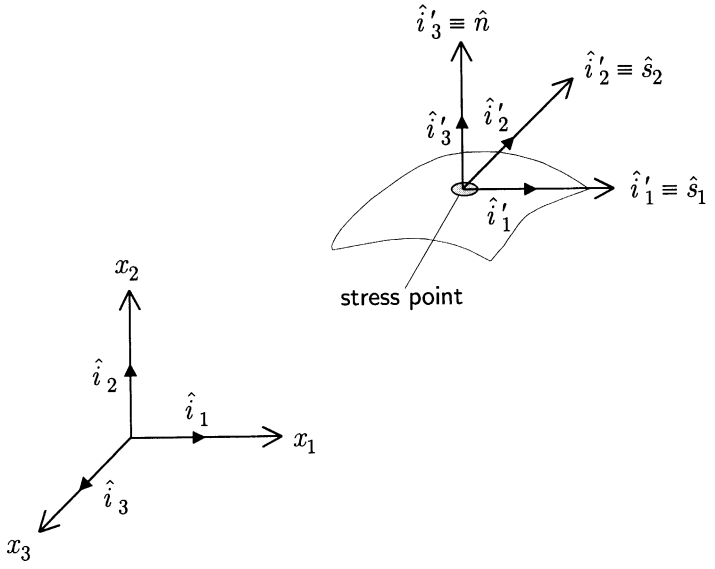

Fig. 2. Three-dimensional boundary element and local Cartesian coordinate system at the boundary point where the stresses are computed.

consideration can be obtained as

$$\epsilon'_{\alpha\beta} = \frac{1}{2}\left(\frac{\partial u'_\alpha}{\partial x'_\beta} + \frac{\partial u'_\beta}{\partial x'_\alpha}\right) = \frac{1}{2}\left[(\hat{s}_\alpha \cdot \hat{i}_m)\frac{\partial u_m}{\partial s_\beta} + (\hat{s}_\beta \cdot \hat{i}_m)\frac{\partial u_m}{\partial s_\alpha}\right]. \tag{21}$$

Also, using Hooke's law and the definition of the traction vector, all the components of the symmetric stress tensor are given by (see Fig. 3)

$$\sigma'_{33} = t'_3 = (\hat{n}\cdot\hat{i}_m)t_m, \tag{22}$$

$$\sigma'_{11} = \frac{1}{1-v}[2\mu(\epsilon'_{11} + v\epsilon'_{22} + v\sigma'_{33}],$$

$$\sigma'_{22} = \frac{1}{1-v}[2\mu(\epsilon'_{22} + v\epsilon'_{11}) + v\sigma'_{33}],$$

$$\sigma'_{13} = \sigma'_{31} = t'_1 = (\hat{s}_1\cdot\hat{i}_m)t_m,$$

$$\sigma'_{23} = \sigma'_{32} = t'_2 = (\hat{s}_2\cdot\hat{i}_m)t_m,$$

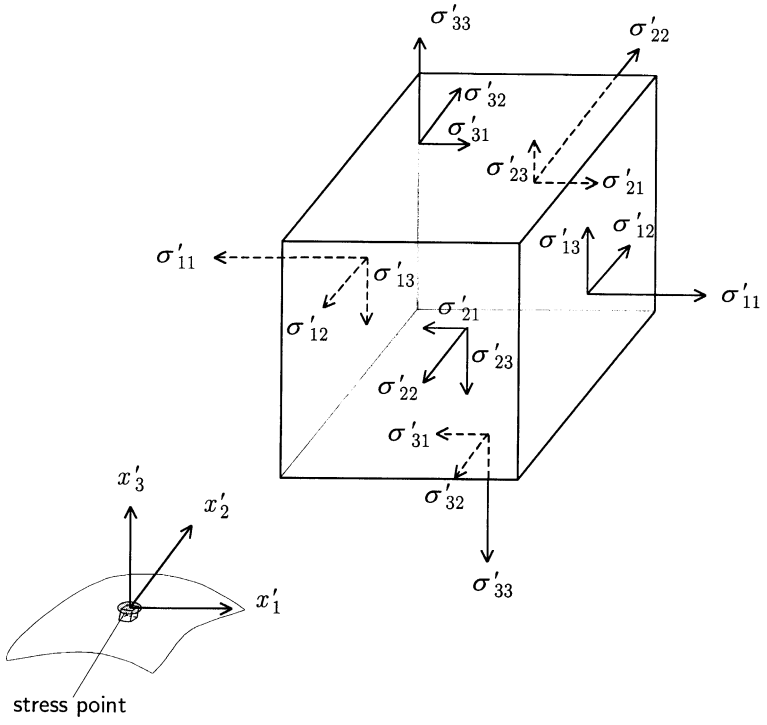

Fig. 3. Components of the stress tensor in terms of a local coordinate system.

$$\sigma'_{12} = \sigma'_{21} = 2\mu\epsilon'_{12}.$$

Thus, once the strain components $\epsilon'_{\alpha\beta}$ are known, the computation of the stresses is straightforward. Unfortunately, the computation of those components of the strain tensor is a little bit involved since in general, at the point under consideration, the values of the tangential derivatives of the displacements $\partial u_i/\partial s_\alpha$ are not directly recovered from the BEM solution.

Using the results presented in Ref. [27], the tangential derivatives of the displacements are given by

$$\frac{\partial u_i}{\partial s_\alpha} = \frac{1}{G}\left[(g_{22}\vec{e}_1 - g_{12}\vec{e}_2)\frac{\partial u_i}{\partial \eta_1} + (g_{11}\vec{e}_2 - g_{21}\vec{e}_1)\frac{\partial u_i}{\partial \eta_2}\right]\cdot\hat{s}_\alpha, \tag{23}$$

where, as before, $\vec{e}_\alpha = (\partial x_i/\partial\eta_\alpha)\vec{i}_i$, $g_{\alpha\beta} = \vec{e}_\alpha\cdot\vec{e}_\beta$, and $G = \det([g_{\alpha\beta}])$.

In the standard BEM, where Lagrangian elements are used for discretization of the boundary, the values of $\partial u_i/\partial\eta_\alpha$ are established using the nodal values of the displacements and the derivatives of the Lagrangian shape functions with respect to the parametric coordinates η_1 and η_2

$$\frac{\partial u_i}{\partial \eta_\alpha} = \sum_{N=1}^{NN}\frac{\partial M^{(N)}}{\partial \eta_\alpha}(\eta_1,\eta_2)u_i^{(N)}. \tag{24}$$

In the above expression, NN is the number of functional nodes in the element, $M^{(N)}$ is the Lagrangian shape function associated with the Nth functional node, and $u_i^{(N)}$ are values of the displacements at the Nth functional node.

In the case of the Hermite-like elements, the values of $\partial u_i/\partial\eta_\alpha$ can be obtained as follows:

$$\begin{aligned}\frac{\partial u_i}{\partial \eta_\alpha}(\eta_1,\eta_2) &= \sum_{N=1}^{NN}\left\{\frac{\partial H_0^{(N)}(\eta_1,\eta_2)}{\partial\eta_\alpha}u_i^{(N)} + \frac{\partial H_1^{(N)}(\eta_1,\eta_2)}{\partial\eta_\alpha}\frac{\partial u_i^{(N)}}{\partial s_1^{(N)}}\right.\\ &\left. + \frac{\partial H_2^{(N)}(\eta_1,\eta_2)}{\partial\eta_\alpha}\frac{\partial u_i^{(N)}}{\partial s_2^{(N)}}\right\}.\end{aligned} \tag{25}$$

In the above expression, NN is the number of functional nodes in the element, $H_k^{(N)}$ $(k = 0, 1, 2)$ are the shape functions associated with the Nth functional node, and $u_i^{(N)}$, $\partial u_i^{(N)}/\partial s_1^{(N)}$, and $\partial u_i^{(N)}/\partial s_2^{(N)}$ are the values of displacements and their tangential derivatives at the Nth functional node.

Once all the components of the stress tensors are determined in the primed system, their counterparts in the unprimed system can be obtained through the use of the well-known transformation law for second order tensors

$$\sigma_{ij} = (\hat{i}'_m\cdot\hat{i}_i)(\hat{i}'_n\cdot\hat{i}_j)\sigma'_{mn}. \tag{26}$$

3. Computation of the error indicator

As in the two-dimensional case (see Ref. [11]), the computation of the error indicator in three-dimensional elastostatic problems is based on measuring the difference between two different numerical solutions for the boundary stresses.

Suppose that for a given problem, a sequence of approximate solutions for the boundary stresses

$$\hat{\sigma}_{ij}^{\{1\}}(\vec{x}), \hat{\sigma}_{ij}^{\{2\}}(\vec{x}), \hat{\sigma}_{ij}^{\{3\}}(\vec{x})\ldots\hat{\sigma}_{ij}^{\{n\}}(\vec{x}) \tag{27}$$

is available, and that $\hat{\sigma}_{ij}^{\{n\}}(\vec{x})$ has more degrees of freedom than $\hat{\sigma}_{ij}^{\{n-1\}}(\vec{x})$. As the number of degrees of freedom increases, it is reasonable to expect that the resulting numerical solution will get closer to the exact solution if the method is converging to the latter. That is, if the sequence will converge to the exact solution as the number of degrees of freedom increases indefinitely then

$$|\sigma_{ij}(\vec{x}) - \hat{\sigma}_{ij}^{\{n\}}(\vec{x})| \to 0 \text{ as } n \to \infty, \tag{28}$$

where $\sigma_{ij}(\vec{x})$ is the exact solution.

If this is the case, then two different approximate solutions in the sequence must approach arbitrarily close to each other, that is

$$|\hat{\sigma}_{ij}^{\{m\}}(\vec{x}) - \hat{\sigma}_{ij}^{\{n\}}(\vec{x})| \to 0 \text{ as } n, m \to \infty \tag{29}$$

since

$$\begin{aligned}&|\sigma_{ij}(\vec{x}) - \hat{\sigma}_{ij}^{\{n\}}(\vec{x})| + |\sigma_{ij}(\vec{x}) - \hat{\sigma}_{ij}^{\{m\}}(\vec{x})|\\ &\quad\geq |[\sigma_{ij}(\vec{x}) - \hat{\sigma}_{ij}^{\{n\}}(\vec{x})] - [\sigma_{ij}(\vec{x}) - \hat{\sigma}_{ij}^{\{m\}}(\vec{x})]|\\ &\quad= |\hat{\sigma}_{ij}^{\{m\}}(\vec{x}) - \hat{\sigma}_{ij}^{\{n\}}(\vec{x})|.\end{aligned} \tag{30}$$

The two approximate solutions with different number of degrees of freedom can be chosen almost arbitrarily as long as they fulfill the basic convergency requirements imposed by the numerical method. In this work, these two different solutions are obtained through the use of Hermite-like and Lagrangian boundary elements (see Fig. 4).

The use of the difference between two numerical solutions to obtain an estimate of the error has been successfully used in the past (see for example Refs. [32,33]). Although effective, the use of two approximate solutions to estimate the error is usually expensive, especially in three-dimensional problems where complex models may involve a relatively large number of elements. Some proposals exist to reduce the cost associated with the computation of the second solution. One is the use of the local reanalysis technique [3]. Another one is to use the values corresponding to the previous solution on all those elements whose reported error is below a certain prescribed value [34].

For two dimensional problems, Muci-Küchler et al. [10] and Muci-Küchler and Miranda-Valenzuela [11] showed that it is possible to obtain two different numerical solutions from only one analysis with Hermite elements. The first

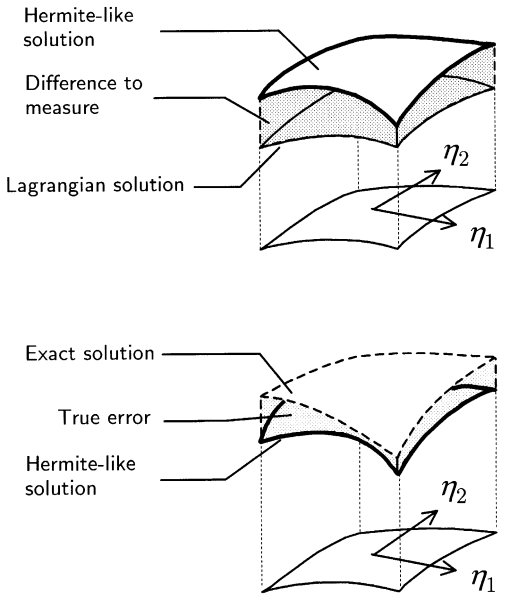

Fig. 4. Comparison between the true error and the difference to be measured (i.e. the approximate error).

solution is the standard solution that is obtained through the use of Hermite elements. The second 'reduced' solution is obtained by considering each Hermite element as a Lagrangian one with the same number and distribution of nodes. Since Hermite elements include in their formulation the conventional degrees of freedom (i.e. the nodal values of the displacements and tractions), it is possible to use those quantities to represent the field variables inside the elements using the shape functions corresponding to a Lagrangian element.

This procedure can also be extended to three-dimensional problems as two different solutions can also be obtained from just one analysis with Hermite-like elements (see Fig. 5). These two solutions can be easily compared to obtain an estimate of the error. The way in which the two solutions are obtained and the error indicator is computed, are detailed in the following sections.

From Eqs. (21) and (22), the computation of the boundary stresses in three dimensions depends on one normal and two tangent vectors, the values for the tractions, and the values for the tangential derivatives of the displacements.

For the Hermite-like solution, the values of $\partial u_i/\partial s_\alpha$ can be determined through the use of Eqs. (25) and (23). Of course, the use of these equations is not necessary if the point of interest is a functional node since the nodal values for the tangential derivatives of the displacements are directly recovered from the BEM solution.

The tractions have also to be interpolated if the point of interest is not a functional node. For the Hermite-like solution the tractions are obtained from

$$t_i(\eta_1,\eta_2)=\sum_{N=1}^{NN}\left\{H_0^{(N)}(\eta_1,\eta_2)t_i^{(N)}+H_1^{(N)}(\eta_1,\eta_2)\frac{\partial t_i^{(N)}}{\partial s_1^{(N)}}+H_2^{(N)}(\eta_1,\eta_2)\frac{\partial t_i^{(N)}}{\partial s_2^{(N)}}\right\}, \tag{31}$$

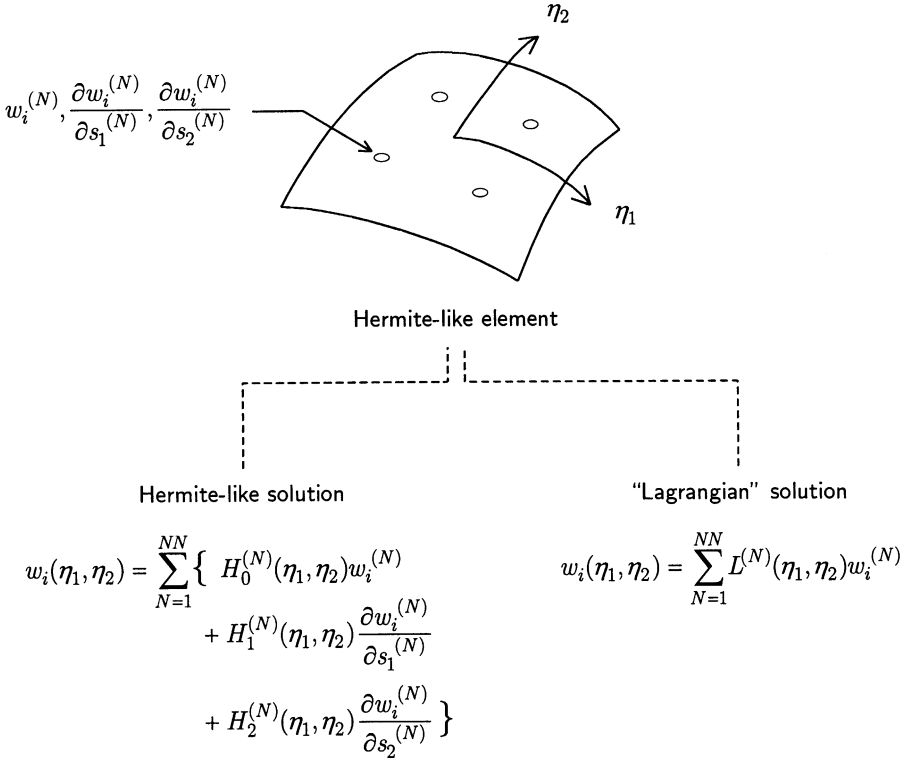

Fig. 5. Obtention of the second 'reduced' solution from the solution with Hermite-like elements.

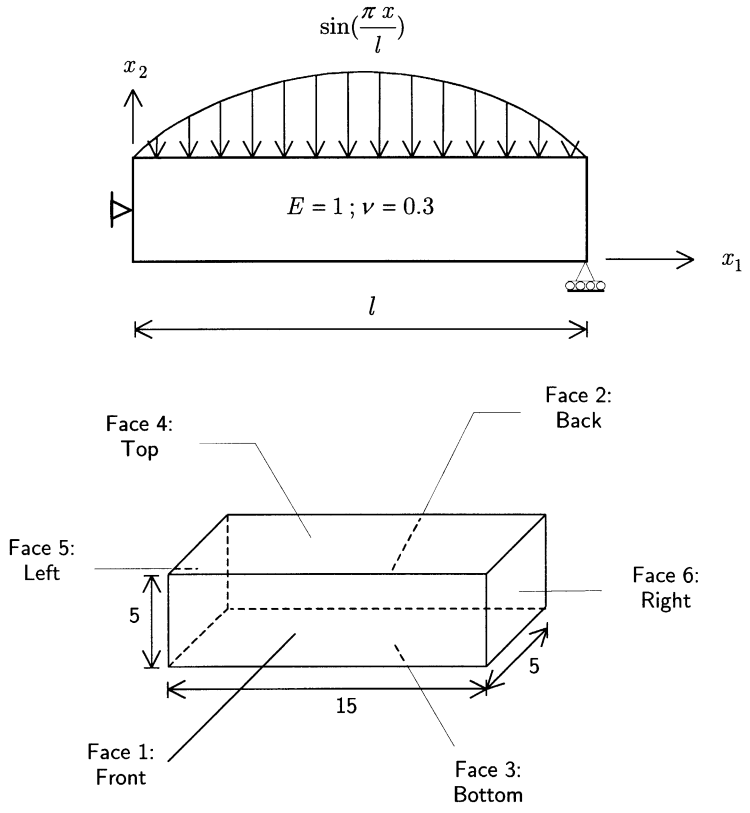

Fig. 6. Boundary value problem and modeled region for Example 1 (Section 4.1).

where $t_i^{(N)}$, $\partial t_i^{(N)}/\partial s_1^{(N)}$, and $\partial t_i^{(N)}/\partial s_2^{(N)}$ are the values of the tractions and their tangential derivatives at the Nth functional node.

For the Lagrangian solution, the values for the tangential derivatives of the displacements always have to be obtained through the differentiation of the functional representation for the displacements using Eqs. (24) and (23).

As for the tractions, they only have to be interpolated if the point of interest is not a functional node

$$t_i(\eta_1, \eta_2) = \sum_{N=1}^{NN} M^{(N)}(\eta_1, \eta_2) t_i^{(N)}. \tag{32}$$

It is important to mention at this point that since the normal and tangent unit vectors depend only on the geometry of the boundary, they will be the same for both solutions since they share the same geometric representation.

If the numerical solution for a specific stress component (or a combined stress measure such as the von Mises stress) corresponding to the Hermite-like elements is denoted as σ, and the numerical solution for the same stress component corresponding the Lagrangian elements is denoted as σ^*, the error indicator for an element 'e' can be computed in the L_2 sense as

$$\lambda_\sigma^{(e)} = \left\{ \int_{-1}^{1} \int_{-1}^{1} [\sigma^{(e)}(\eta_1, \eta_2) - \sigma^{*(e)}(\eta_1, \eta_2)]^2 J(\eta_1, \eta_2)\, \mathrm{d}\eta_1\, \mathrm{d}\eta_2 \right\}^{1/2}, \tag{33}$$

where $J(\eta_1,\eta_2)$ is the Jacobian of the geometric transformation.

Up to this point, nothing has been said about which specific stress component is considered in Eq. (33). Although the formulation of the error indicator opens the possibility of using any stress component to estimate the error in the solution, some quantities may be more convenient than others. Quantities such as the von Mises stress, the maximum principal stress, the minimum principal stress, or the maximum shear stress, may prove more useful since they are commonly used in the design of mechanical components to evaluate the risk of mechanical failure. The need of estimating the error in quantities of real interest has also been expressed by other authors like Strouboulis et al. [35].

4. Numerical examples

To illustrate the behavior and applicability of the new error indicator proposed here, three different numerical

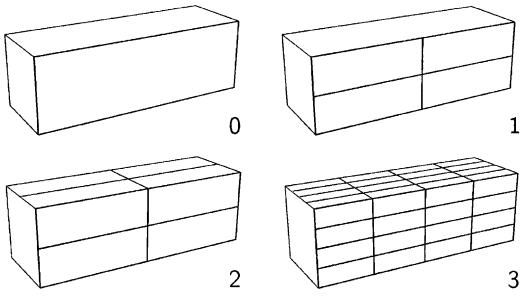

Fig. 7. Meshes corresponding to the adaptive process for Example 1 (Section 4.1).

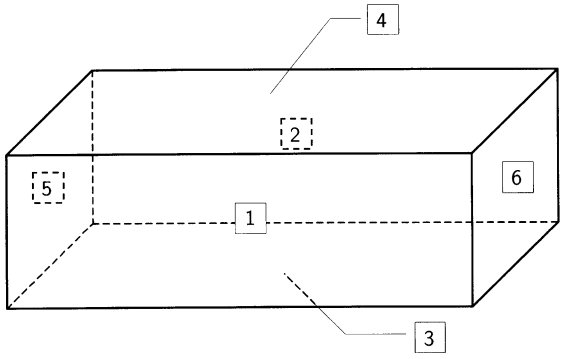

Fig. 8. Labels of the elements used to report the results shown in Fig. 9 for to the initial mesh of Example 1 (Section 4.1).

examples are presented. The first one is a simply supported beam subject to continuously distributed sinusoidal load acting on its top surface. The second example corresponds to the axisymmetric problem of a thick wall cylinder subject to an internal pressure. The third one is an infinite plate with a circular hole subject to a uniaxial traction applied at infinity. Appropriate boundary conditions are prescribed on all models to ensure that a state of plane strain prevails inside the continuum. The analytical solution for the first problem can be found in Ref. [27]. The analytical solution for the second and third problems can be found in Ref. [36].

For all the models used in the three examples, the field variables are approximated using only non-isoparametric, quadrilateral, completely discontinuous, Hermite-like boundary elements with four nodes. Although completely discontinuous elements provide the best versatility for the adaptation of the mesh, they have the disadvantage of adding new non-shared nodes every time an element is refined.

4.1. Example 1: simply supported beam subject to a continuously distributed sinusoidal load

The first example is that of a simply supported beam subject to a continuously distributed sinusoidal load acting on its top surface. Fig. 6 shows the cross-section of the beam in the $x1x2$ plane, the applied load, and the modelled region. The values corresponding to the analytical solution provided in Ref. [27] are used to specify some of the boundary conditions for the model. The front and back faces of the beam are subject to the conditions $t_1 = 0$, $t_2 = 0$, and $u_3 = 0$, and the bottom surface is traction free. Also, on the top surface the tractions are specified as $t_1 = 0$, $t_2 = -\sin(\pi x/l)$, For the left face of the beam, the displacement u_1 is specified using the values obtained from the analytical solution, and the remaining conditions are given as $u_2 = 0$ and $t_3 = 0$. Finally, for the right face of the model, the conditions $t_1 = 0$, $u_2 = 0$, and $t_3 = 0$ are prescribed.

For this problem, the error in the numerical solution was estimated in the von Mises stress. As refinement criteria, all those elements with a value for the error indicator larger than 0.7 times the maximum value for the same quantity were divided into four elements of equal size. The adaptive process was stopped after three steps were completed.

The adaptive process for this problem is presented in Fig. 7. For all the meshes shown in the figure, the number and

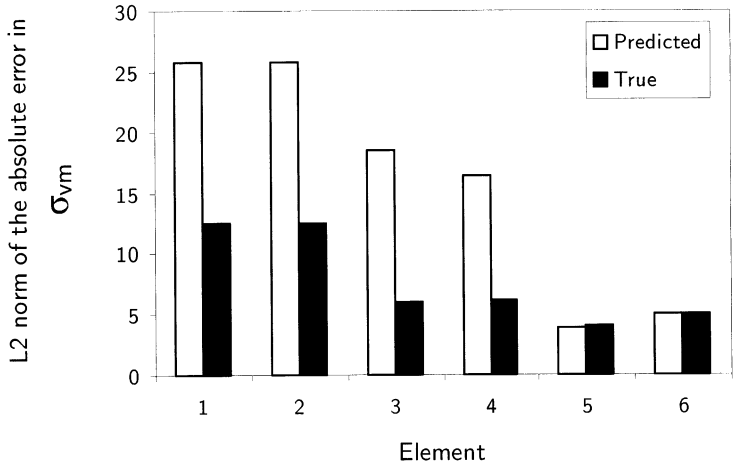

Fig. 9. Comparison of the predicted and true errors in the von Mises stress for the initial mesh of the adaptive process corresponding to Example 1 (Section 4.1).

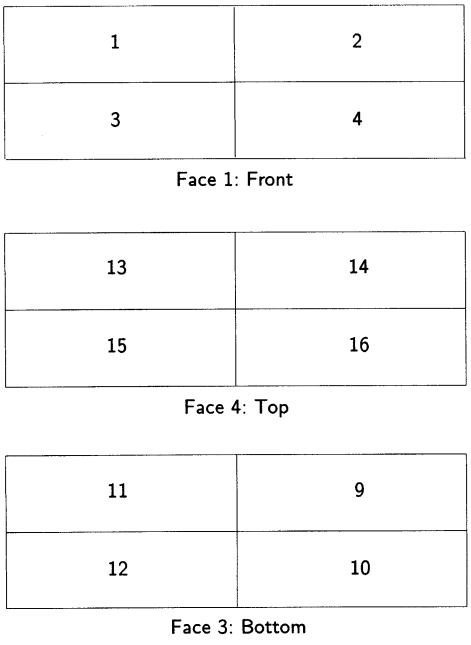

Fig. 10. Labels of the elements used to report the results shown in Figs. 11–13 for Mesh 2 of Example 1 (Section 4.1).

distribution of the elements in the hidden faces is exactly the same as the one on the corresponding opposite faces. Also, it is important to point out that the way in which the elements are refined along faces 1–4 is a direct consequence of the symmetric loading of the beam and the two-dimensional nature of the problem.

Using the element labels shown in Fig. 8, a comparison of the L_2 norm of the predicted and true errors in the von Mises stress for the elements of the initial mesh is presented in Fig. 9. As can be seen, the error indicator reasonably tracks the behavior of the true error in all the elements of the initial mesh.

The behavior of the proposed error indicator can be verified further using Mesh 2 of the adaptive process. Based on the element labels given in Fig. 10, Figs. 11–13 plot the values of the L_2 norm of the predicted and true errors in the von Mises stress for the elements on the top, bottom, and front faces of the model, respectively. From the figures it is clear that the error indicator keeps providing a good account on how the true error is behaving. However, it is evident that in this case the error indicator considerably overestimates the true error in all the elements. The use of completely discontinuous elements could be one of the causes of this considerable overestimation.

In Fig. 14, the behavior of the maximum value of the L_2 norm of the predicted and true errors in the von Mises stress at each step of the adaptive process is presented. This figure shows that both, the predicted and true errors, diminish and tend to zero with each step. Also, the figure shows that, for this example, the maximum predicted error for the elements in the mesh is an upper bound of the maximum true error at each step of the adaptive process. Furthermore, it is interesting to note the abrupt change in the slope of the curve after the second step. This abrupt change is due to the large number of elements that were refined in the second step as a consequence of most elements having a similar error. Finally, it is clear from the figure that the last step of the adaptive process is not really needed since the maximum true error for Mesh 2 is already very small.

4.2. Example 2: thick wall cylinder subject to internal pressure

The second example is a thick wall cylinder subject to an internal pressure. The boundary value problem and modeled region for this example are shown in Fig. 15. The specified boundary conditions for this problem are as follows. The front and back faces of the cylinder, and the outer surface (face 4), are subject to the conditions $t_1 = 0$, $t_2 = 0$ and $u_3 = 0$. In the bottom part of the model (face 3), the conditions $t_1 = 0$, $u_2 = 0$, and $u_3 = 0$ are prescribed. For the left

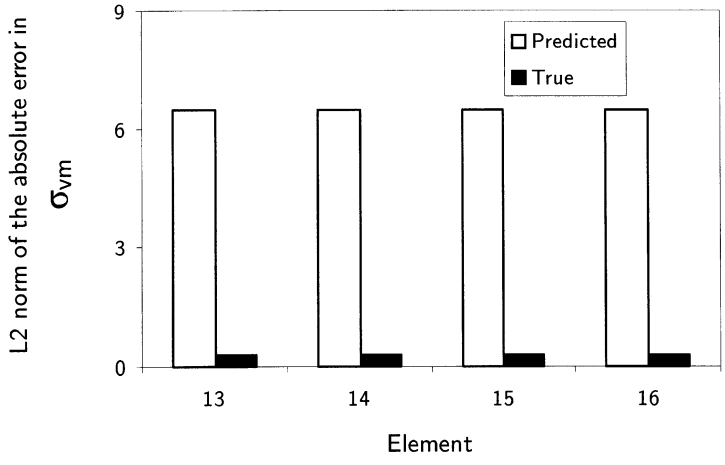

Fig. 11. Comparison of the predicted and true errors in the von Mises stress on the top face of Mesh 2 of the adaptive process corresponding to Example 1 (Section 4.1).

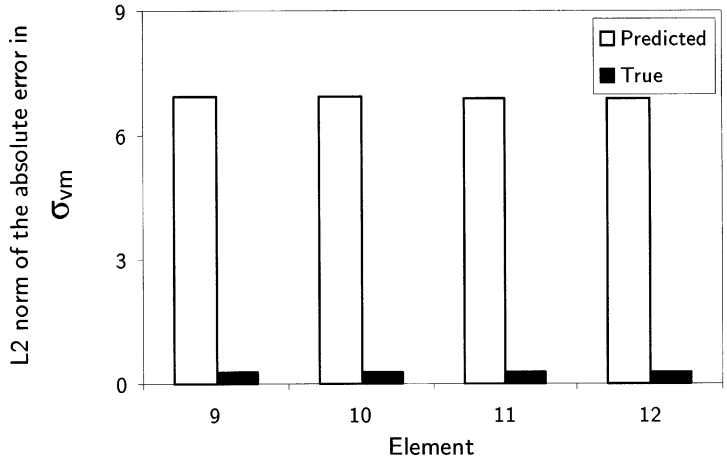

Fig. 12. Comparison of the predicted and true errors in the von Mises stress on the bottom face of Mesh 2 of the adaptive process corresponding to Example 1 (Section 4.1).

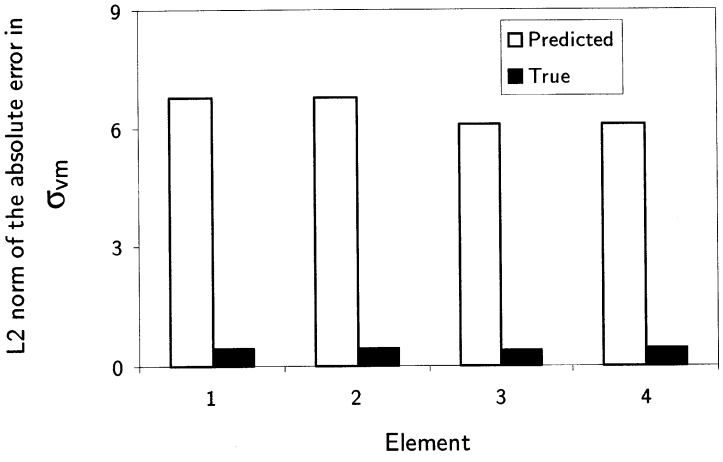

Fig. 13. Comparison of the predicted and true errors in the von Mises stress on the bottom face of Mesh 2 of the adaptive process corresponding to Example 1 (Section 4.1).

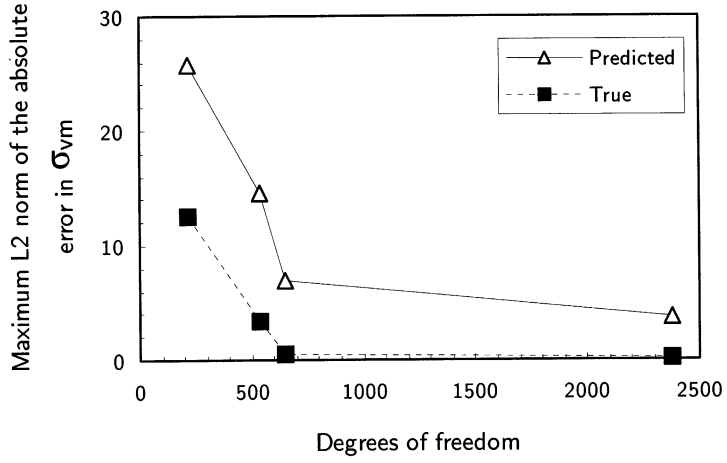

Fig. 14. Behavior of the maximum values for the predicted and true errors in the von Mises stress during the adaptive process corresponding to Example 1 (Section 4.1).

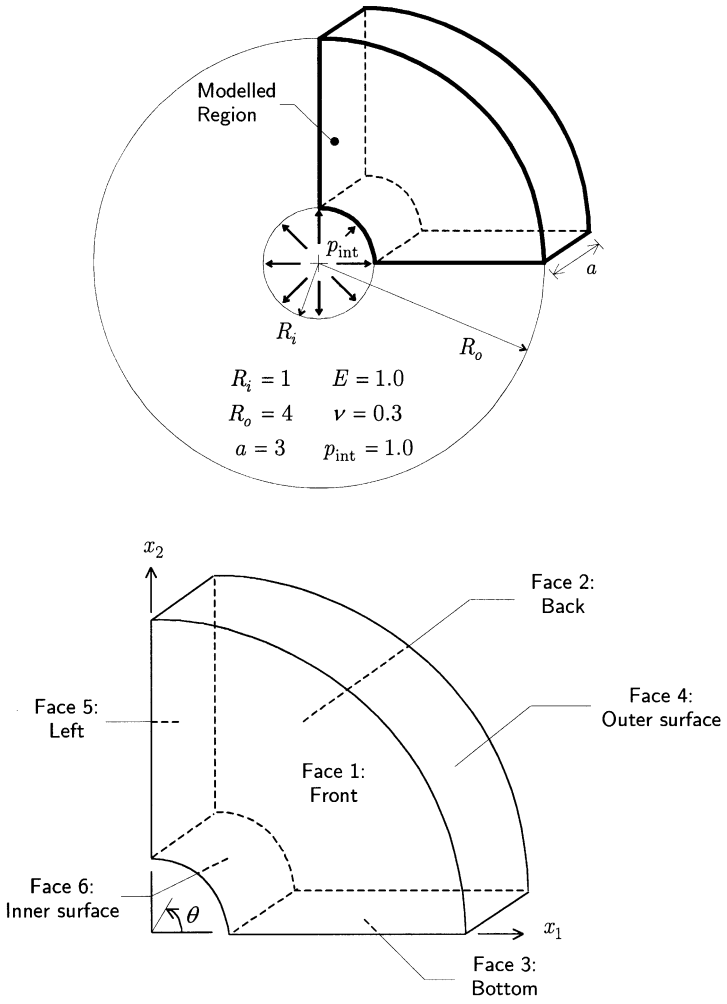

Fig. 15. Boundary value problem and modeled region for Example 2 (Section 4.2).

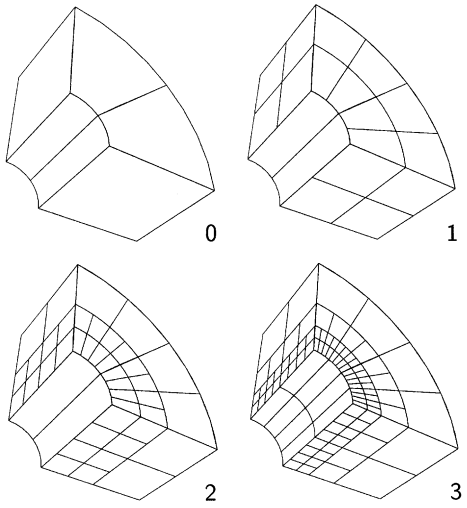

Fig. 16. Meshes corresponding to the adaptive process for Example 2 (Section 4.2).

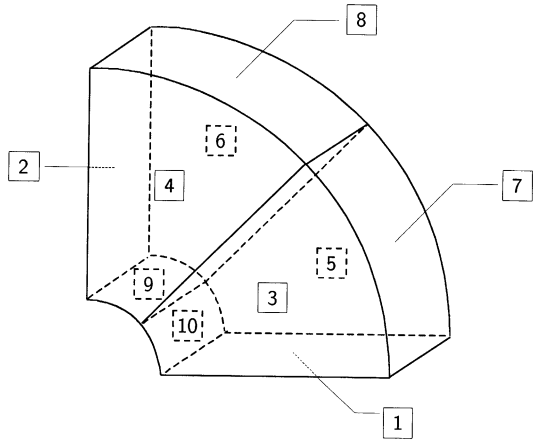

Fig. 17. Labels of the elements used to report the results shown in Fig. 18 for the initial mesh of Example 2 (Section 4.2).

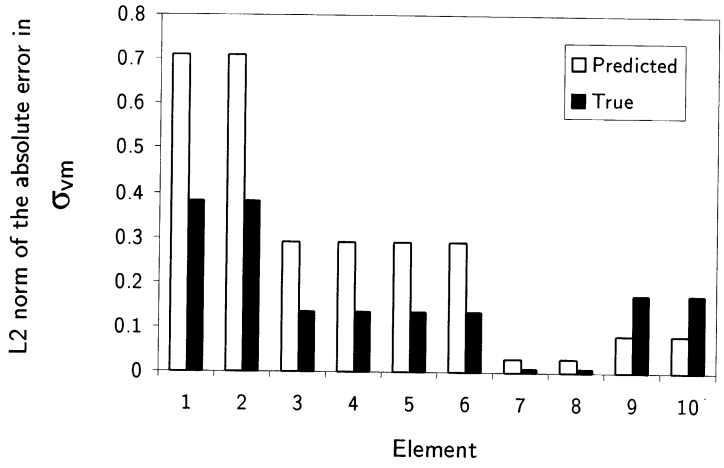

Fig. 18. Comparison of the predicted and true errors in the von Mises stress for the initial mesh of the adaptive process corresponding to Example 2 (Section 4.2).

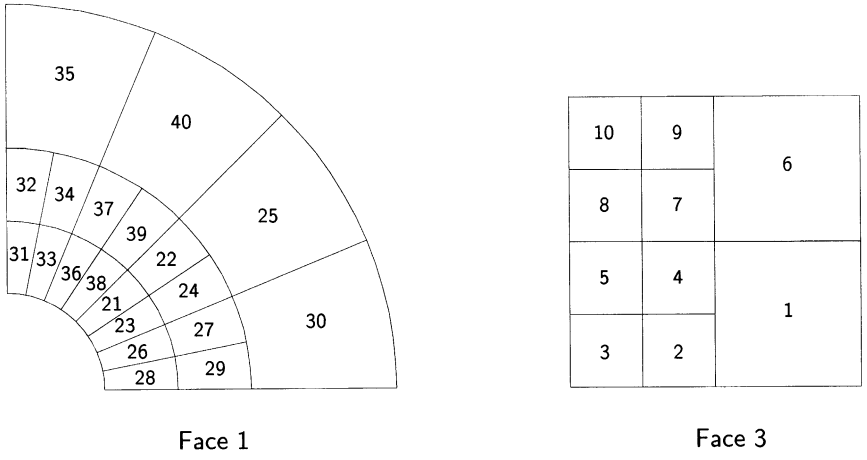

Fig. 19. Labels of the elements used to report the results shown in Figs. 20 and 21 for Mesh 2 of Example 2 (Section 4.2).

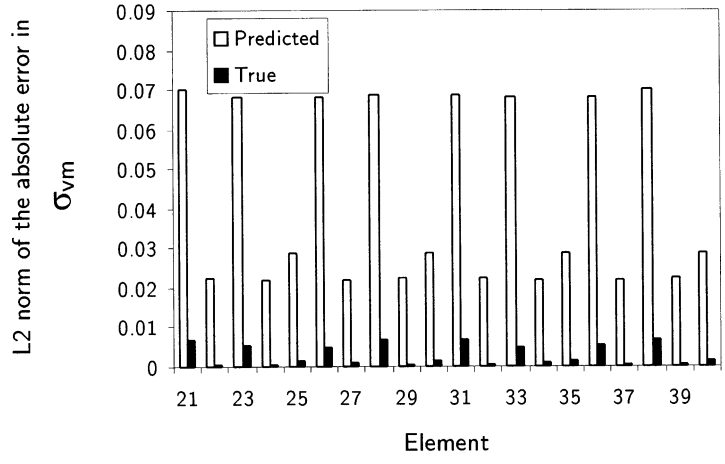

Fig. 20. Comparison of the predicted and true errors in the von Mises stress for the front face of Mesh 2 of the adaptive process corresponding to Example 2 (Section 4.2).

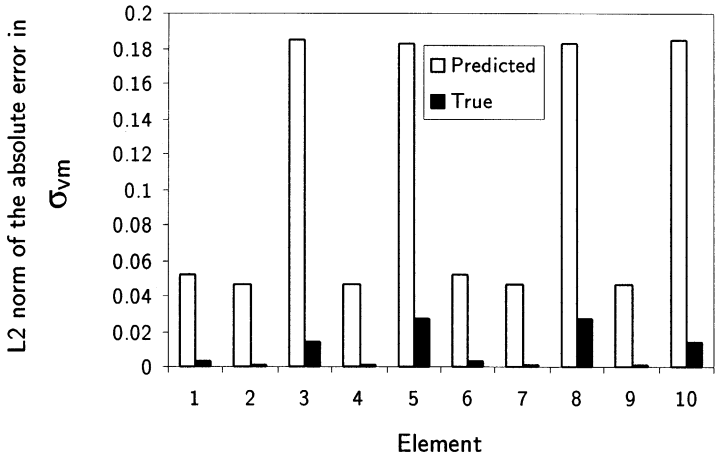

Fig. 21. Comparison of predicted and true errors in the von Mises stress for the bottom face of Mesh 2 of the adaptive process corresponding to Example 2 (Section 4.2).

boundary of the model (face 5), the conditions $u_1 = 0$, $t_2 = 0$, and $u_3 = 0$ are specified. Finally, for the inner curved surface (face 6), the conditions $t_1 = p_{\text{int}} \cos\theta$, $t_2 = p_{\text{int}} \sin\theta$, and $u_3 = 0$ are prescribed.

For this problem, the error was estimated in the von Mises stress and, as refinement criteria, all those elements with a value for the error indicator larger than the average value for the same quantity were divided into four elements of equal size.

The adaptive process for this problem is presented in Fig. 16. The initial mesh was constructed using only 10 Hermite-like boundary elements, just enough to describe the geometry and the boundary conditions. The geometry of the model was represented using linear elements in faces 3 and 5, and 8-noded quadratic elements elsewhere. As can be seen in the figure, three adaptive steps were performed.

From Fig. 16 it is easy to see that the resulting refinement distribution agrees with the behavior of the analytical solution for the problem under consideration. Since the problem is axisymmetric, the solution for the von Mises stress is constant along the inner and outer curved surfaces. Hence, few or no refinement at all occurs on these boundaries (in the case of the outer surface, not shown in the figure, no refinement took place during the adaptive process). Along the radial direction, the von Mises stress distribution has the highest gradients towards the inner curved surface, which accounts for the finer mesh near that portion of the boundary. Finally, as can be expected, the refinement is symmetric due to the nature of the analytical solution.

Using the element labels given in Fig. 17, a comparison between the L_2 norm of the predicted and true errors in the von Mises stress for each element of the initial mesh is presented in Fig. 18. This plot shows how the error indicator 'points out' those elements with the largest error, namely, elements 1 and 2 which correspond to the bottom and left faces of the model, respectively. Furthermore, it gives a reasonable idea of the behavior of the true error in the mesh. Two exceptions are elements 9 and 10, which have a predicted error smaller than the true error. This may be a consequence of the very coarse mesh used as the starting point for the adaptive process.

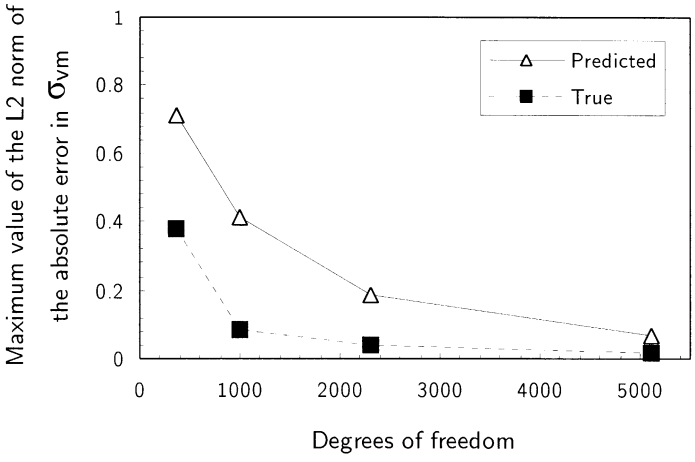

Fig. 22. Behavior of the maximum values for the predicted and true errors in the von Mises stress during the adaptive process corresponding to Example 2 (Section 4.2).

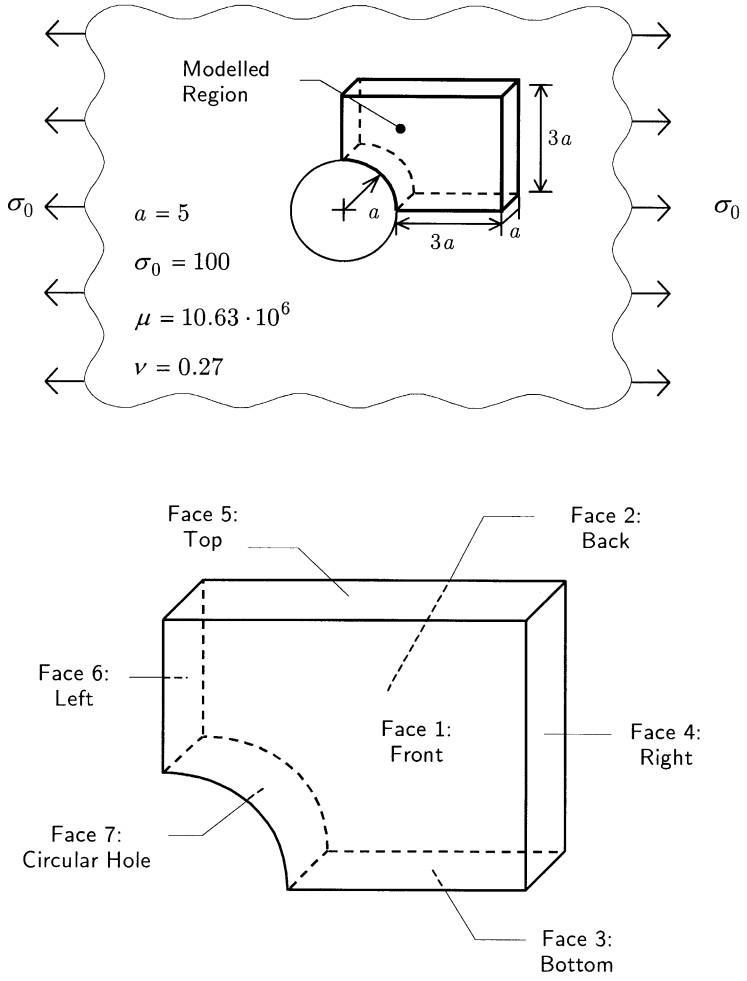

Fig. 23. Boundary value problem and modeled region for Example 3 (Section 4.3).

Using the element label shown in Fig. 19 for the elements of Mesh 2, Figs. 20 and 21 show the behavior, in the L_2 norm, of the predicted and true errors in the von Mises stress for the front and bottom faces of that mesh. Once more, the error indicator points out those elements with the largest error. From both plots it is clear that the error indicator is over predicting the true error in the elements. As mentioned before, this behavior could be related in part to the use of discontinuous elements. Although not shown, for this mesh the value of the predicted error for the elements lying on the inner face of the model was 0.1. This value was approximately twice and a half times the value for the true error in those elements.

It is interesting to point out that in Fig. 21 the values for the true error in elements 3, 5, 8, and 10 are not the same. From the nature of the problem under consideration it seems reasonable to expect very similar, if not equal, values for these four elements. These differences in the values for the true error are due to very small variations in the numerical results obtained from the BEM solution. These small variations may be a consequence of the roundoff errors in the digital computer due to the use of single precision to run the

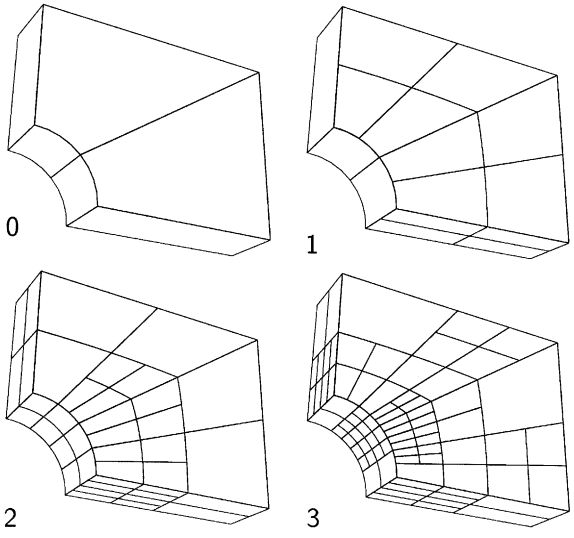

Fig. 24. Meshes corresponding to the adaptive process for Example 3 (Section 4.3).

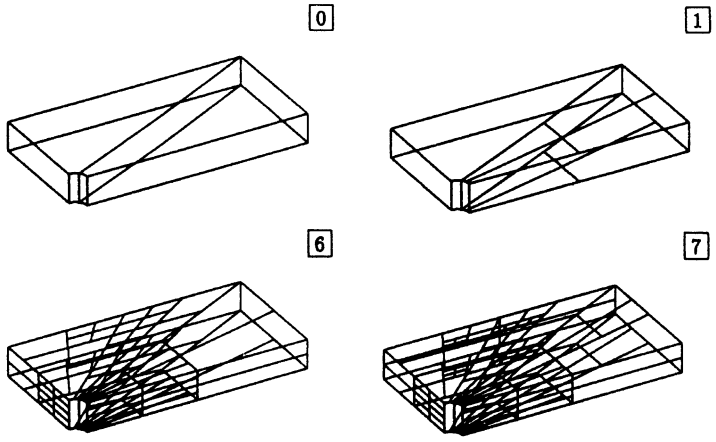

Fig. 25. Initial and final meshes corresponding to the adaptive process carried out by Crook and Smith [19] for the problem of Example 3 (Section 4.3).

BEM analysis code. The motivation to use single precision to run the code is to demonstrate that the formulation used in this paper to implement the Hermite-like elements is robust and stable.

The behavior of the maximum values for the L_2 norm of the predicted and true errors in the von Mises stress during the adaptive process is shown in Fig. 22. For this problem, the predicted error is an upper bound of the true error at every step of the adaptive process. As expected, both tend to zero as the mesh is refined. It should be kept in mind that for this simple problem, the refinement of the mesh is no longer needed beyond the second step where very close values to the ones corresponding to the analytical solution are obtained. The additional step is presented to show the correct behavior of the adaptive process.

4.3. Example 3: infinite plate with a circular hole subject to an uni-axial traction

The third example is an infinite plate with a circular hole subject to an uni-axial traction applied at infinity. As shown in Fig. 23, taking into account the symmetry of the problem, only one quarter of the domain is analyzed. Since the modeled region is only a small part of the infinite plate, appropriate boundary conditions are applied using the results provided by the analytical solution. The boundary conditions are specified as follows. The front and back faces of the plate, and the inner surface corresponding to the circular hole, are subject to the conditions $t_1 = 0$, $t_2 = 0$, and $u_3 = 0$. In the bottom surface (face 3), the conditions $t_1 = 0$, $u_2 = 0$, and $u_3 = 0$ are prescribed. The left surface of the model (face 6) is subject to the conditions $u_1 = 0$, $t_2 = 0$, and $u_3 = 0$. Finally, on the right and top surfaces of the model, the values of t_1 and t_2 are specified using the values obtained from the analytical solution for the problem, and $u_3 = 0$.

As in the previous examples, the error indicator for this problem was based on the von Mises stress. The initial mesh consisted of 10 Hermite-like elements with 4 nodes. The geometry of the surfaces corresponding to the bottom, right, top and left faces was represented using linear elements. The geometry of the front, back and inner faces was approximated using eight-noded quadratic elements.

The adaptive process was run for three steps and, as refinement criteria, all those elements whose value for the error indicator was larger than the average value for the same quantity were divided in four elements of equal size.

The initial mesh and the meshes corresponding to each step of the adaptive process are shown in Fig. 24. Although not shown in Fig. 24, the top and right faces of the model were not refined in the first two steps. In the final mesh, namely Mesh 3, these two surfaces have 4 elements each. These four meshes compare well with results obtained for the same problem in two dimensions using Hermite elements [11]. They also agree with the results obtained by Crook and Smith [19] for the same problem in three dimensions using discontinuous Lagrangian elements (see Fig. 25).

Based on the element labels shown in Fig. 26, a comparison between the L_2 norm of the predicted and true errors in

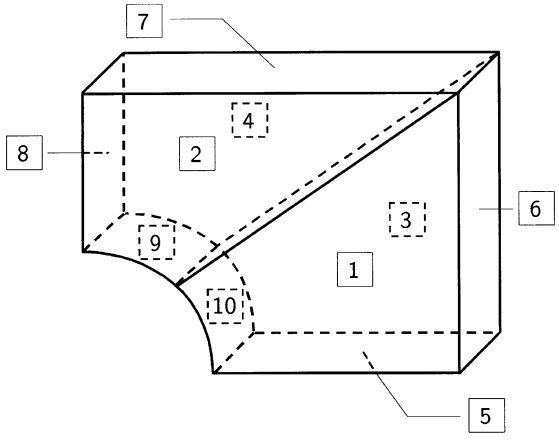

Fig. 26. Labels of the elements used to report the results shown in Fig. 27 corresponding to the initial mesh of the adaptive process for Example 3 (Section 4.3).

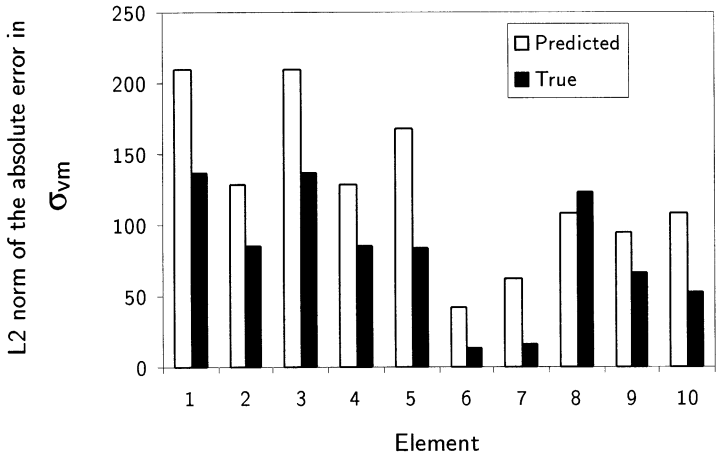

Fig. 27. Comparison of predicted and true errors in the von Mises stress for the initial mesh of the adaptive process corresponding to Example 3 (Section 4.3).

the von Mises stress for the initial mesh is presented in Fig. 27. This plot shows a behavior for the error indicator similar to the one observed in the two previous examples. With the exception of element 8, the error indicator points out all those elements with the largest error. It should be noted, however, that in the following step of the adaptive process element 8 was refined.

In Fig. 28, the element labels for Mesh 2 of the adaptive process are shown. With reference to this figure, the values for the L_2 norm of the predicted and true errors in the von Mises stress for the elements of Mesh 2 are compared in Figs. 29–32. In general, a reasonable agreement in the behavior between the predicted and true error for the different parts of the mesh exists, although some exceptions occur. These discrepancies are most noticeable in the bottom part of the model (face 3) and the boundary corresponding to the cylindrical surface of the circular hole (face 7), as shown in Fig. 32.

It should be stressed that the cost involved in the computation for the error indicator is very small, especially if compared with the total cost of the BEM analysis. This low computational cost makes the error indicator particularly suitable to lead adaptive processes.

The behavior of the maximum values for the L_2 norm of

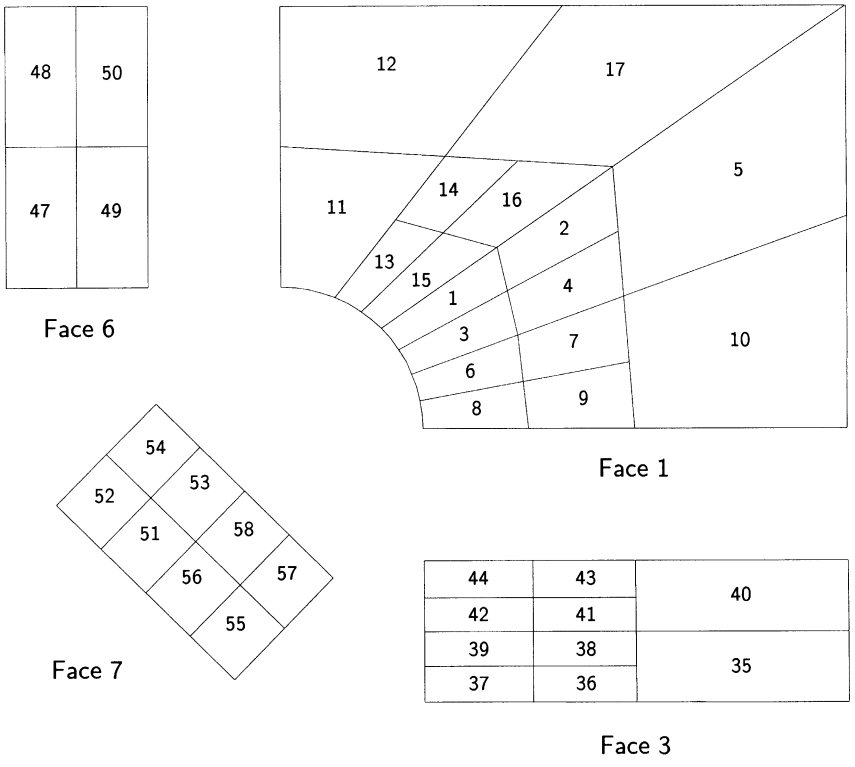

Fig. 28. Labels of the elements used to report the results shown in Figs. 29–32 for Mesh 2 of Example 3 (Section 4.3).

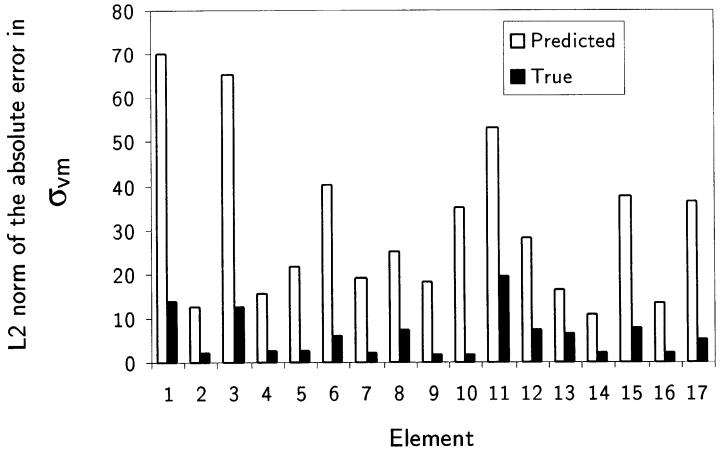

Fig. 29. Comparison of predicted and true errors in the von Mises stress for the front face of Mesh 2 of the adaptive process corresponding to Example 3 (Section 4.3).

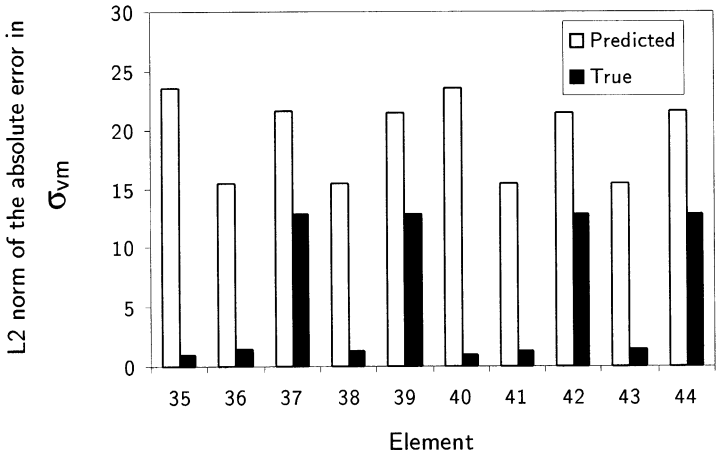

Fig. 30. Comparison of predicted and true errors in the von Mises stress for the bottom face of Mesh 2 of the adaptive process corresponding to Example 3 (Section 4.3).

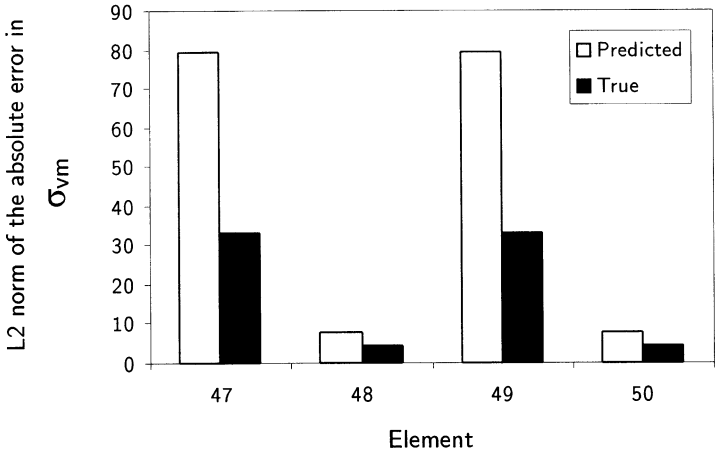

Fig. 31. Comparison of predicted and true errors in the von Mises stress for the left face of Mesh 2 of the adaptive process corresponding to Example 3 (Section 4.3).

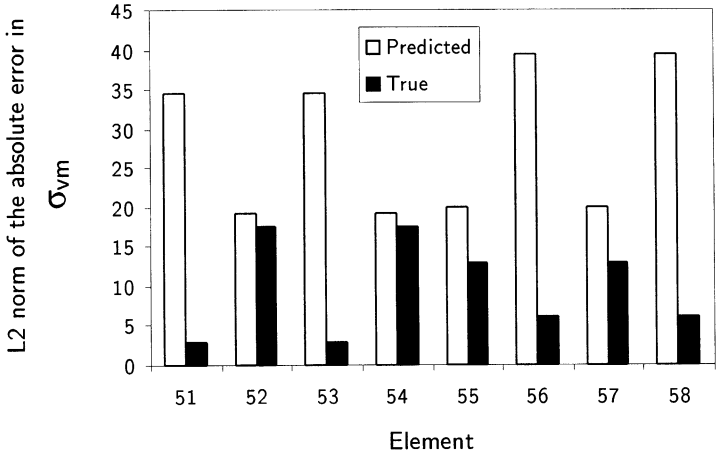

Fig. 32. Comparison of predicted and true errors in the von Mises stress for the surface of the hole of Mesh 2 of the adaptive process corresponding to Example 3 (Section 4.3).

the predicted and true errors in the von Mises stress at each step of the adaptive process is shown in Fig. 33. As expected, both tend to zero as the mesh is refined. The predicted error is also an upper bound for the true error with the exception of Mesh 1. The under prediction of the true error at this step may be due to the introduction of new elements, and therefore, more refined boundary conditions. This might be an indication that the starting mesh was too coarse. A similar behavior was obtained by Crook and Smith in their analysis [19].

5. Conclusions

In this paper, a new error indicator based on stresses for three-dimensional elastostatic problems was presented. Its formulation was based on the possibility of obtaining two different numerical solutions for the stresses from just one analysis with Hermite-like boundary elements. Since the two numerical solutions needed to compute an estimate of the error in the elements of a given mesh were obtained from the same BEM analysis, the computational cost associated with the new error indicator was very low. The three numerical examples that were presented showed that the error indicator was capable of tracking in a reasonable fashion the behavior of the true error and that, in most cases, it gave an upper bound for it. The good balance between reliability and efficiency provided by the error indicator made it very suitable to lead the adaptive processes. In addition, we believe that the opportunity to estimate the error in the solution using quantities like the von Mises (or other stress component) may be appealing to designers and analysts since these quantities are commonly used to predict mechanical failure.

Although the formulation for the Hermite-like boundary elements and the error indicator that was presented can be used for continuous, partially discontinuous, or discontinuous elements with any number of nodes, discontinuous quadrilateral elements with four nodes were used to facilitate the implementation of the mesh refinement algorithm.

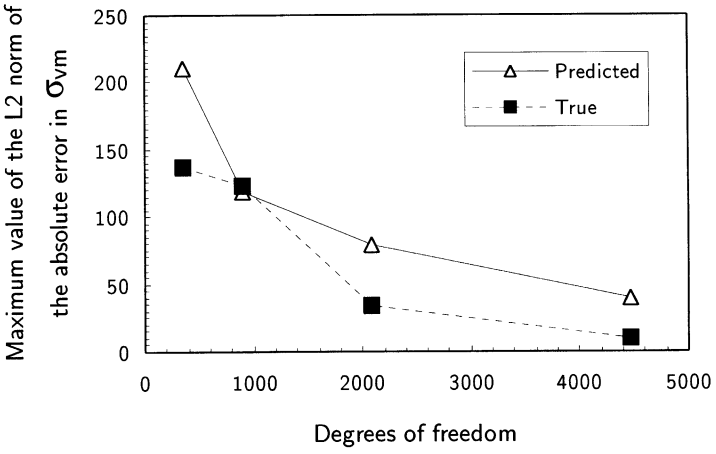

Fig. 33. Behavior of the maximum values for the predicted and true errors in the von Mises stress during the adaptive process corresponding to Example 3 (Section 4.3).

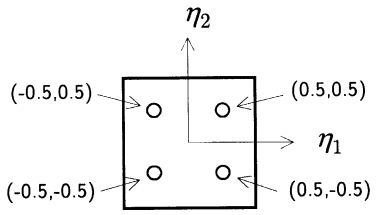

Fig. 34. Discontinuous Hermite-like boundary element with four nodes.

Of course, the use of discontinuous elements considerably increases the number of degrees of freedom in the model, without necessarily increasing the accuracy in the numerical results obtained at all those locations of the boundary where all the stress components are continuous. Thus, a remeshing scheme that could use as much as possible, continuous elements should be advantageous. Likewise, the possibility of dividing the elements according to the direction of the largest error could be of interest as less degrees of freedom would be introduced at each step of the adaptive process. Finally, the ideas presented here can be easily extended to other problems were a suitable formulation for Hermite-like elements is available.

Acknowledgements

José C. Miranda-Valenzuela acknowledges the financial support provided by CONACyT, the Mexican National Council for Science and Technology, for the realization of this work.

Appendix. Shape functions for Hermite-like elements

As an example, the geometry-independent shape functions corresponding to the completely discontinuous quadrilateral Hermite-like boundary element with four nodes shown in Fig. 34 are given by

$$\hat{H}_0^{(1)}(\eta_1,\eta_2) = -\tfrac{1}{4}(2\eta_1-1)(2\eta_2-1)[\eta_1(2\eta_1+1) + \eta_2(2\eta_2+1)-1],$$

$$\hat{H}_1^{(1)}(\eta_1,\eta_2) = -\tfrac{1}{16}(2\eta_1+1)(2\eta_2-1)(2\eta_1-1)^2,$$

$$\hat{H}_2^{(1)}(\eta_1,\eta_2) = -\tfrac{1}{16}(2\eta_1-1)(2\eta_2+1)(2\eta_2-1)^2,$$

$$\hat{H}_0^{(2)}(\eta_1,\eta_2) = \tfrac{1}{4}(2\eta_1+1)(2\eta_2-1)[\eta_1(2\eta_1-1) + \eta_2(2\eta_2+1)-1],$$

$$\hat{H}_1^{(2)}(\eta_1,\eta_2) = -\tfrac{1}{16}(2\eta_1-1)(2\eta_2-1)(2\eta_1+1)^2,$$

$$\hat{H}_2^{(2)}(\eta_1,\eta_2) = \tfrac{1}{16}(2\eta_1+1)(2\eta_2+1)(2\eta_2-1)^2,$$

$$\hat{H}_0^{(3)}(\eta_1,\eta_2) = -\tfrac{1}{4}(2\eta_1+1)(2\eta_2+1)[\eta_1(2\eta_1-1) + \eta_2(2\eta_2-1)-1],$$

$$\hat{H}_1^{(3)}(\eta_1,\eta_2) = \tfrac{1}{16}(2\eta_1-1)(2\eta_2+1)(2\eta_2+1)^2,$$

$$\hat{H}_2^{(3)}(\eta_1,\eta_2) = \tfrac{1}{16}(2\eta_1+1)(2\eta_2-1)(2\eta_2+1)^2,$$

$$\hat{H}_0^{(4)}(\eta_1,\eta_2) = \tfrac{1}{4}(2\eta_1-1)(2\eta_2+1)[\eta_1(2\eta_1+1) + \eta_2(2\eta_2-1)-1],$$

$$\hat{H}_1^{(4)}(\eta_1,\eta_2) = \tfrac{1}{16}(2\eta_1+1)(2\eta_2-1)(2\eta_1-1)^2,$$

$$\hat{H}_2^{(4)}(\eta_1,\eta_2) = -\tfrac{1}{16}(2\eta_1-1)(2\eta_2-1)(2\eta_2+1)^2. \quad \text{(A1)}$$

References

[1] Liapis S. A review of error estimation and adaptivity in the boundary element method. Engng Anal 1994;14:315–23.
[2] Kita E, Kamiya N. Recent studies on adaptive boundary element methods. Adv Engng Software 1994;19:21–32.
[3] Charafi A, Neves AC, Wrobel LC. h-Hierarchical adaptive boundary element method using local reanalysis. Int J Numer Methods Engng 1995;38:2185–207.
[4] Guiggiani M. Sensitivity analysis for boundary element error estimation and mesh refinement. Int J Numer Methods Engng 1996;39:2907–20.
[5] Paulino GH, Shi F, Mukherjee S, Ramesh P. Nodal sensitivities as error estimates in computational mechanics. Acta Mech 1997;121:191–213.
[6] Gallego R, Martínez-Castro A, Suarez J. In: Aliabadi MH, editor. Sensitivity analysis of approximate solutions for the hypersingular boundary element method, Boundary Elements Techniques Conference, London, UK, 1999. 1999. p. 311–9.
[7] Paulino GH, Gray LJ, Zarikian V. Hypersingular residuals — a new approach for error estimation in the boundary element method. Int J Numer Methods Engng 1996;39:2005–29.
[8] Liang MT, Chen JT, Yang SS. Error estimation for boundary element method. Engng Anal 1999;23:257–65.
[9] Menon G, Paulino GH, Mukherjee S. Analysis of hypersingular residuals error estimates in boundary element methods for potential problems. Comput Methods Appl Mech Engng 1999;173:449–73.
[10] Muci-Küchler KH, Miranda-Valenzuela JC, Rudolphi TJ. A new error indicator for adaptive meshing with Hermite Boundary Elements. Comput Methods Appl Mech Engng 1999;173:419–31.
[11] Muci-Küchler KH, Miranda-Valenzuela JC. A new error indicator based on stresses. Engng Anal 1999;23:657–70.
[12] Miranda-Valenzuela JC, Muci-Küchler KH, Soriano-Soriano S. In: Aliabadi MH, editor. Adaptive meshing in thermoelasticity using Hermite boundary elements, Boundary Elements Techniques Conference, London, UK, 1999. p. 261–72.
[13] Watson JO. In: Banerjee PK, Watson JO, editors. Hermitian cubic and singular elements for plane strain, Developments in boundary element methods, vol. 4. London: Elsevier, 1986 (Chapter 1).
[14] Rudolphi TJ. The use of simple solutions in the regularization of hypersingular integral equations. Math Comput Model 1991;15:269–78.
[15] Muci-Küchler KH, Rudolphi TJ. Coincident collocation of displacement and tangent derivative boundary integral equations in elasticity. Int J Numer Methods Engng 1993;36:2837–49.

[16] Muci-Küchler KH, Hernández-Luna JA. Formulation of higher order boundary elements for the solution of steady state thermoelastic problems. Paper presented at the 24th Midwestern Mechanics Conference. Ames, Iowa, USA, 1995.
[17] Cerrolaza M, Alarcon E. p-Adaptive boundary elements for three-dimensional potential problems. Comm Appl Numer Methods 1987;3:335–44.
[18] Liapis S. An adaptive boundary element method for the solution of potential flow problems. Engng Anal 1996;18:29–37.
[19] Crook SH, Smith RNL. Conforming and non-conforming elements in a three-dimensional H-adaptive boundary element method. In: Brebbia CA, Gipson GS, editors. Boundary elements, vol. XIII. Amsterdam: Elsevier, 1991. p. 929–42.
[20] Ervin VJ, Stephan EP. Adaptive approximations for 3-D electrostatic plate problems. Adv Engng Software 1992;15:211–5.
[21] Demkowicz L, Karafiat A, Oden TJ. Solution of elastic scattering problems in linear acoustics using h–p boundary element Meth. Comput Methods Appl Mech Engng 1992;101:251–82.
[22] Karafiat A. On hp-error estimation in the BEM for a three-dimensional Helmholtz exterior problem. Comput Methods Appl Mech Engng 1997;150:199–214.
[23] Yokoyama M, Zhan J. A p-adaptive 3-D BEM for acquiring the desired accuracy. Adv Engng Software 1997;28:395–401.
[24] Yokoyama M, Kanoh T. Accuracy estimation of the 3-D BEM analysis of elastostatic problems by the zooming method. Adv Engng Software 2000;31:355–65.
[25] Bächtold M, Korvink JG, Baltes H. An error indicator and automatic adaptive meshing for 3D electrostatic boundary element simulations. In: Marchetti M, Brebbia CA, Aliabadi MH, editors. Boundary element methods, vol. XIX. Computational Mechanics Publications, 1997. p. 709–18.
[26] Kamiya N, Kawaguchi K. An adaptive BEM by sample point error analysis. Engng Anal 1992;9:225–62.
[27] Muci-Küchler KH, Rudolphi TJ. Application of tangent derivative boundary integral equations to the formulation of higher order boundary elements. Int J Solid Struct 1994;31:1565–84.
[28] Tomlinson K, Bradley C, Pullan A. On the choice of a derivative boundary element formulation using Hermite interpolation. Int J Numer Methods Engng 1996;39:451–68.
[29] Pullan AJ, Bradley CP. A coupled cubic hermite finite element/boundary element procedure for electrocardiographic problems. Comput Mech 1996;18:356–68.
[30] Becker AA. The boundary element in engineering — a complete course. New York: McGraw-Hill, 1992.
[31] Liu Y, Rudolphi TJ. Some identities for fundamental solutions and their applications to non-singular boundary element formulations. Engng Anal 1991;8:301–11.
[32] Rencis JJ, Mullen RL. Solution of elasticity problems by a self-adaptive mesh refinement technique for boundary element computation. Int J Numer Methods Engng 1986;23:1509–27.
[33] Rencis JJ, Mullen RL. A self adaptive mesh refinement technique. Comput Mech 1988;3:309–19.
[34] Rodríguez JJ, Power H. A mesh refinement technique for the boundary element method based on local error analysis. In: Brebbia CA, Power H, editors. Boundary elements, vol. XXI. WIT Press, 1999. p. 291–302.
[35] Strouboulis T, Babuška I, Datta DK, Copps K, Gangaraj SK. A posteriori estimation and adaptive control of the error in the quantity of interest. Part I: A posteriori estimation of the error in the von Mises stress and the stress intensity factor. Comput Methods Appl Mech Engng 2000;181:261–94.
[36] Timoshenko SP, Goodier JN. Theory of elasticity. 3rd ed. New York: McGraw-Hill, 1970.
[37] Huebner KH, Thorton EA. The finite element method for engineers. 2nd ed. Wiley/Interscience, 1982.